Acoustic Assisted Actuation of Ni–Mn–Ga Ferromagnetic Shape Memory Alloys

by

Bradley William Peterson

Submitted to the Department of Materials Science and Engineering
in partial fulfillment of the requirements for the degree of

Doctor of Philosophy in Materials Science and Engineering

at the

MASSACHUSETTS INSTITUTE OF TECHNOLOGY

September 2006

Author .....
Department of Materials Science and Engineering
August 9, 2006

Certified by .....
Samuel M. Allen
POSCO Professor of Physical Metallurgy
Thesis Supervisor

Certified by .....
Robert C. O'Handley
Senior Research Scientist
Thesis Supervisor

Accepted by .....
Samuel M. Allen
Chairman, Department Committee on Graduate Students

Acoustic Assisted Actuation of Ni–Mn–Ga Ferromagnetic Shape Memory Alloys

by

Bradley William Peterson

Submitted to the Department of Materials Science and Engineering
on August 9, 2006, in partial fulfillment of the
requirements for the degree of
Doctor of Philosophy in Materials Science and Engineering

Abstract

Ferromagnetic shape memory alloys (FSMA) have been shown in recent work to exhibit large magnetic field induced strains. The material generally requires a large threshold field (of order 3–4 kOe) to initiate the strain. Thus, the power requirements are large and actuators based on these materials could tend to be large. This thesis reports on the effect on the actuation properties of Ni–Mn–Ga single crystals of the use of a sinusoidal stress wave generated by a piezoelectric stack actuator.

The piezoelectric drive causes a time varying stress wave in the FSMA that resolves as a shear across the twin-boundaries and aids the twin boundary in overcoming defect-related obstacles. The FSMA shows increased strain and a reduction in threshold field. The effect is most pronounced for crystals showing large initial threshold fields which are associated with high defect strengths or concentrations. For crystals with a large threshold, 4.7 kOe, actuated at 1 Hz, the piezoelectric drive reduces the threshold field by as much as 21% for a piezoelectric driven at 5 kHz and 20 V_{rms}. As a result of this large threshold reduction, strain output can be more than doubled for magnetic drive amplitudes near the threshold field. Strain improvement is modest, 0.001, for magnetic field drive amplitudes that are near saturation magnetization.

The effect of piezo-assisted actuation as a function of the magnetic drive frequency was also investigated. The apparatus was first modeled using finite element simulations to determine its expected resonant behavior. The actuation behavior of the high-frequency apparatus was then tested at Ni–Mn–Ga actuation frequencies up to 500 Hz. It was found that the strain amplification at constant piezoelectric drive tends to decrease with increasing actuation frequency. Maximum benefit is seen for actuation frequencies under 20 Hz and is believed to be the result of both a reduction in piezoelectric energy input per FSMA actuation cycle at elevated actuation frequencies, and the system dynamics.

The change in piezoelectric drive performance as a function of temperature was investigated for temperatures below the martensitic transformation, 0–30 °C. Strain output decreases with temperature as a result of lowered twin-boundary mobility. The piezoelectric drive does yield an improvement in strain response for all temperatures

investigated, however the effect is maximized at 12.5 °C which is near the inflection point of increasing field-induced strain with temperature.

Thesis Supervisor: Samuel M. Allen
Title: POSCO Professor of Physical Metallurgy

Thesis Supervisor: Robert C. O'Handley
Title: Senior Research Scientist

Acknowledgments

First, I'd like to thank my advisors, Bob O'Handley and Sam Allen, for their support over the years. Graduate school is often ripe with horror stories of difficult advisors and miserable experiences as a result. I have none of those stories. They are a wonderful pair of advisors that are easy to work with, have always available when needed, and have been immeasurable help.

I'd also like to thank my thesis committee members, Yet-Ming Chiang and Christopher Schuh, for their advice on my thesis and help in presenting my results to a wider audience.

Many thanks go out to the other members of the magnetic materials group. Jorge Feuchtwanger provided many hours of assistance throughout the lab on a huge range of topics from "carbon" to electronics. Marc Richard was invaluable for his knowledge of crystal structure and microscopy, especially in regards to Ni–Mn–Ga defects. Miguel Marioni deserves recognition for getting me interested in this field and for being a mentor during my initial stay at MIT. I'd like to thank David Bono for his practice knowledge of electronic and magnetic devices as well as Joshua Chambers, Jesse Simon, and Ratchatee Techapiesancharoenkij for their general helpfulness and sense of humor.

No acknowledgements would be complete without mentioning my parents, who have always been there to support and encourage me as long as I can remember. And special thanks to Maura Lee, for being an active motivator over the last few years and all her love and support.

Contents

List of Figures

List of Tables

Chapter 1

Introduction

The ferromagnetic shape memory alloy (FSMA), with nominal composition Ni_2MnGa, was first postulated to exhibit magnetic-field-induced strain response in 1993 [1, 2]. Measurements conducted in 1996 at MIT demonstrated that a strain of 0.2% at -8 °C in a single crystal could be induced by magnetic fields of a few kOe [3, 4]. Strains of 0.3% were demonstrated in 1999 by Wu, et al. [5]. James showed 4.0% [6] and Tickle reported 4.3% strain [7]. Murray showed near-theoretical strain values were achievable when he reported 6% quasi-static strain in $Ni_{49.8}Mn_{28.5}Ga_{21.7}$ [8]. Recently, strains of 9.5% have been shown in the orthorhombic seven-layered martensitic phase by Sosinov [9]. These reported strains are one to two orders of magnitude greater than can be realized in other field-actuated materials such as piezoelectrics or magnetostrictors. This justifies the wide interest in FSMAs for possible actuator applications.

1.1 Crystallography and Phase Transitions

Ni_2MnGa is an intermetallic compound exhibiting the Heusler structure. Below 800 °C, the material has the $L2_1$ ordering and $Fm\bar{3}m$ crystal symmetry as shown in Figure 1-1. Above 800 °C, the gallium and manganese sites become disordered and the $B2$ ordering is present [10].

As the material is cooled, the $L2_1$ structure undergoes a martensitic transformation from cubic to a tetragonal, $I4/mmm$ structure. The martensitic transition

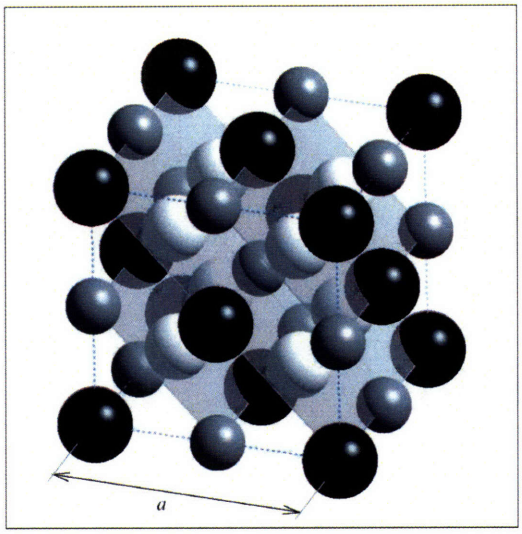

Figure 1-1: The $Fm\bar{3}m$ crystal structure of Ni_2MnGa. The corner positions are gallium (dark grey), the other octahedral sites are manganese (light grey), and the interior tetragonal sites are nickel (white). The [110] planes shown become the twin-planes in the martensitic phase [11].

is characterized as a first order, diffusionless, shear transformation from a higher-symmetry, high temperature structure to a lower-symmetry structure at lower temperatures [12]. The structure is shown in Figure 1-2b along with the parent austenite crystal structure in Figure 1-2a. During the transformation, there is a contraction along one of the austenite a-axes and an expansion in the two perpendicular a-axes directions. The martensite unit cell is redefined relative to the austenite unit cell, however the crystallographic axes in the martensite phase are often referenced to the austenite phase in the literature such that $c < a$. This convention is used for convenience as the maximum theoretical strain is therefore $\epsilon_{max} = 1 - \frac{c}{a}$. This literature convention is also used in this thesis.

The first-order martensitic transformation is a hysteretic process, characterized by the austenite start and finish temperatures, and the martensite start and finish temperatures as shown in Figure 1-3. For temperatures between the austenite start, T_a^s, and the martensite start temperature, T_m^s, the phase present will depend on thermal history.

During the transformation process from austenite to martensite, the transforma-

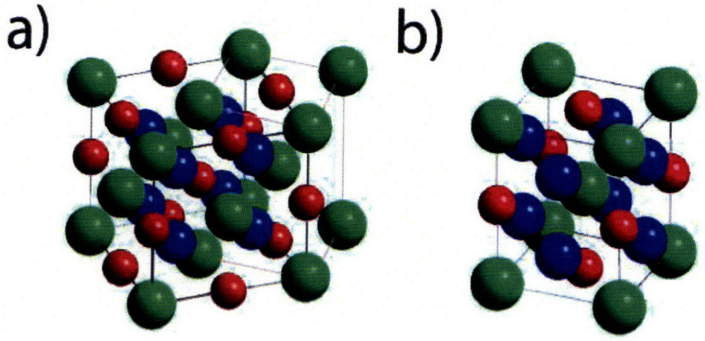

Figure 1-2: Austenite crystal structure (a) showing the martensitic unit cell. (b) shows the martensite $I4/mmm$ unit cell (figure courtesy of M. Richard).

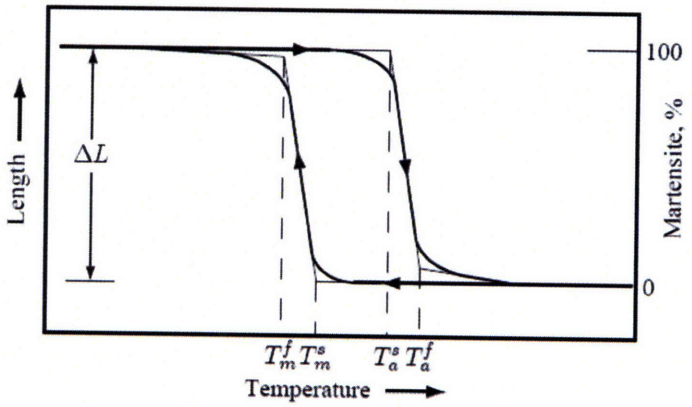

Figure 1-3: The transformation hysteresis for a general martensitic phase transition in a shape memory alloy. Pure martensite exists at low temperature and pure austenite exists at high temperatures [13].

tion stresses from the lattice distortion are often accommodated by the formation of twin-variants [13] as depicted in Figure 1-4. These variants allow for the relief of strain energy within the crystal [14]. The boundary between these two variant regions is referred to as the twin-boundary or twin-plane and many such boundaries can exist in a single crystal. In tetragonal Ni–Mn–Ga, the twin planes lie preferentially along $\{h0h\}$ or $\{0hh\}$ planes and thus separate twin-variants have their c-axis roughly 90° to one another. The boundaries can be moved by the application of a stress, creating a macroscopic shape change. The presence of these boundaries gives rise to the shape memory effect, as they allow for the accommodation of various strain states relative to the initial cubic phase. Regardless of the material's variant arrangement in the

martensitic state, heating of the sample back through the austenite finish temperature will always return it to the original, cubic austenitic structure.

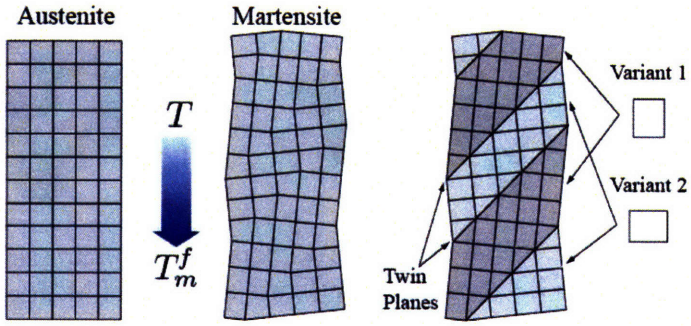

Figure 1-4: During cooling, Ni–Mn–Ga transforms from cubic austenite to tetragonal martensite. In doing so, internal stresses are relieved by the formation of twin-variants [15].

1.2 Magnetic Properties

Ni–Mn–Ga exhibits a strong magnetocrystalline anisotropy with the easy axis oriented parallel to the martensitic c-axis. In the absence of an external magnetic field or external constraints, two twin variants (variant #1 and #2) in the crystal are of equivalent energies (Figure 1-5). In the presence of an external magnetic field, oriented along one of the c-axis, the energy difference, $\Delta G = U_{\parallel}^{eq} - U_{\perp}^{eq}$, between the variants will grow. The divergence in energy with increasing field stabilizes the variant whose c-axis is oriented parallel to the external field. This energy difference between the two variants will continue to grow until all of the magnetic moments in the material are aligned parallel to the magnetic field at the anisotropy field, H_a. The maximum energy difference, which occurs for $H \geq H_a$, will be equal to the anisotropy energy, K_u. Therefore, supplying additional magnetic fields larger than H_a offers no additional driving force and wastes energy.

It is this large magnetocrystalline anisotropy ($K_u \approx 1.7 \pm 0.2 \times 10^5$ J/m^3), in the martensitic phase, which differentiates a FSMA from a traditional shape memory alloy (SMA). The magnetic anisotropy allows for the magnetic field to be used as a

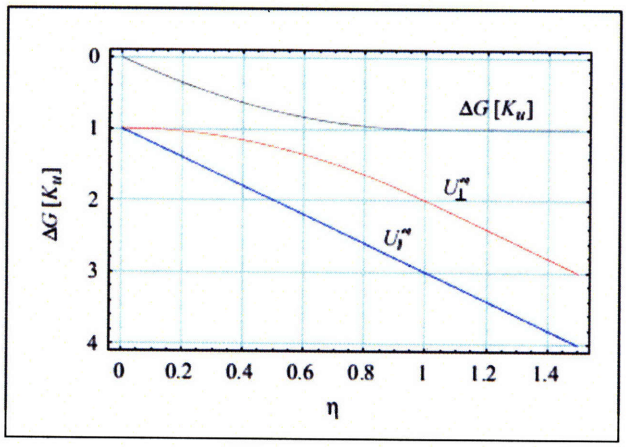

Figure 1-5: Energy difference, ΔG, between the twin-variant aligned, $U_{\parallel}^{eq}$, and perpendicular, $U_{\perp}^{eq}$, to the applied magnetic field in terms of the reduced field $\eta = \frac{H}{H_a}$ [11].

driving mechanism to move twin-boundaries.

1.2.1 Temperature Effects on Magnetic Properties

The magnetic properties of Ni–Mn–Ga are sensitive to temperature, especially in the temperature regions showing magnetic-field-induced strain (MFIS). The material exhibits a Curie temperature of approximately 80–100 °C for the commonly used compositions near $Ni_{50}Mn_{28}Ga_{22}$. Above this temperature, the material is paramagnetic. Figure 1-6 shows the magnetization and anisotropy constant for the 5M, tetragonal martensite. Both quantities rise with a decrease in temperature as thermal fluctuations of the magnetic moments are reduced. Also, as is common in uniaxial materials, the magnetization initially rises faster than the anisotropy as the alloy is cooled below the Curie temperature. The dependence can be expressed mathematically by a power law, such that

$$[m(T)]^3 = \left[\frac{M(T)}{M(0)}\right]^3 = \frac{K_1(T)}{K_1(0)} \tag{1.1}$$

where $m(T)$ is the normalized magnetization at temperature T and $K_1(T)$ is the anisotropy [16, 17]. The anisotropy determines the maximum driving force that can be applied magnetically, and therefore the largest driving forces can be applied at low

temperatures.

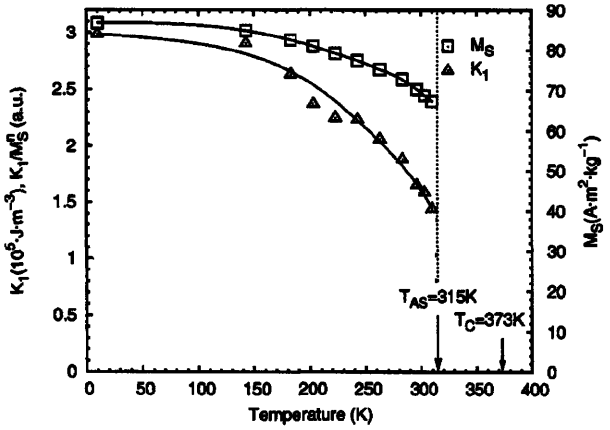

Figure 1-6: Magnetization and anisotropy constant of a 5M tetragonal martensite of composition $Ni_{49.7}Mn_{29.1}Ga_{21.2}$ [17].

1.3 Mechanical Properties

Shape memory alloys have a unique, pseudo-plastic, stress-strain response. Under the application of an applied load, they show an initial stiff elastic region for small strain values (Figure 1-7). After a critical stress value is reached (the threshold stress or twin-boundary yield stress), the applied load causes twin boundary motion and variant rearrangement. During this period, the material stiffness can be orders of magnitude lower than in the initial elastic region. After the variants have swept through the material (approximately $\epsilon > 6\%$ in Figure 1-7), the material becomes stiff again. The sharp changes in stress in the flat region of the curve from $\approx$0.5–6% strain are a result of twin-boundary interactions with defects in the material. The stress builds up when a twin-boundary becomes blocked on a defect or defects. Once the stress build up to sufficient level, the defect is overcome the measured stress drops as the crystal strains under the applied load.

Dai et al. [18] have measured the elastic constants for $Ni_{0.50}Mn_{0.284}Ga_{0.216}$ in a single variant state from 200K to 428K (Figure 1-8). They find that the stiffness increases as the specimen is cooled, until $\approx$220K where a phase change occurs.

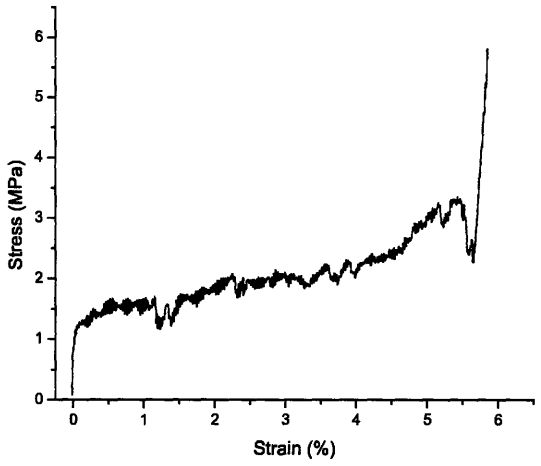

Figure 1-7: Stress-strain for the compression of a single-variant sample of Ni–Mn–Ga (TL7) along the [100] direction. The stiffness in the twinning region is 34.6 MPa.

The material stiffness acts as a resistance to twin-boundary motion, so therefore the twin-boundaries are most mobile when the material stiffness is minimized. This occurs for higher temperatures, in contrast to the driving force which is minimized at high temperatures. The interplay of these two quantities will be discussed further in Chapter 7.

Heczko and Straka [20] report on the twinning stress in 5M tetragonal martensite from 100–307 K as shown in Figure 1-9. They find an exponential increase in the twinning stress with a reduction in temperature. This strong temperature dependence of the twinning stress, which is suggestive of thermally-activated twin-boundary motion, limits the operating range of the FSMA as $K_1 > \sigma_{TW}\epsilon_0$ for MFIS to occur. They also find a larger fraction of untransformed, residual variants at lower temperature and that the magnetic field required to cause 1% strain increases with a decrease in temperature.

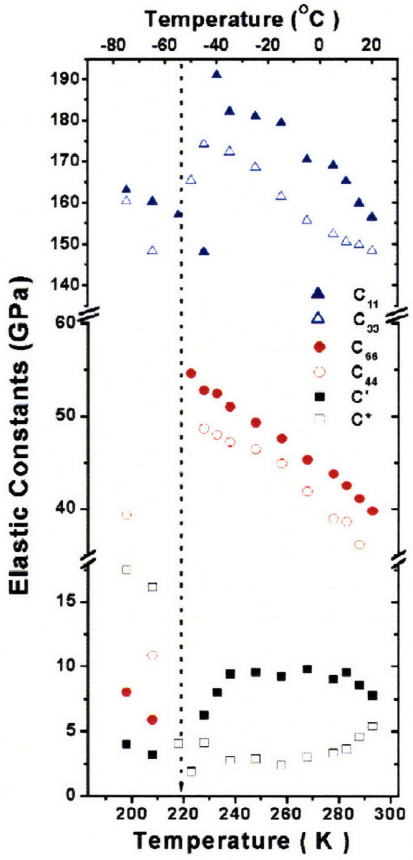

Figure 1-8: Temperature dependence of six elastic constants of $Ni_{0.50}Mn_{0.284}Ga_{0.216}$ below the first martensitic transformation temperature [19, 18].

1.4 Magnetic-field-induced strain response

1.4.1 Quasi-static strain response

Ni_2MnGa has a high magnetocrystalline anisotropy that couples the magnetic easy axis to the crystal's c-axis. For samples with K_u greater than the stress required to initiate twin-boundary motion, an applied magnetic field is capable of moving twin-boundaries and causing a twin variant rearrangement. Under an applied magnetic field, twin boundaries will move so that twin variants with their magnetic easy axis (c-axis) parallel to the applied field will grow in volume fraction. This twin variant rearrangement is what leads to a macroscopic strain that is observed and as can be seen in the upper right frames in Figure 1-10.

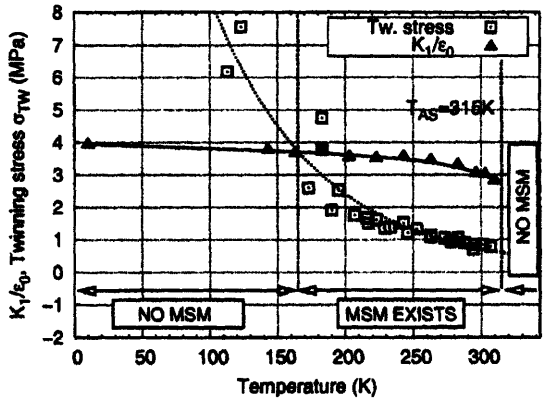

Figure 1-9: Temperature dependence of the twinning stress. MSM refers to the existence of the magnetic shape memory effect which only occurs in the martensite phase for $K_1 > \sigma_{TW}\epsilon_0$ [20].

Murray investigated the effect of an external static load on the strain behavior of $Ni_{49.8}Mn_{28.5}Ga_{21.7}$ [21]. For low stress values, 0.34 MPa, full strain was achieved on the application of a 800 kA/m magnetic field and the strain persisted with the removal of the magnetic field. For intermediate stress values, 0.78–1.62 MPa, large strain was achieved upon application of the magnetic field, and the stress was sufficient to cause partial to full reset of the crystal back to its original strain state. At the larger stress values, 1.63–2.73 MPa, the stress is too large for the magnetic field to work against and the overall strain is low. It can also be seen that as the stress is increased, strain onset (threshold) occurs at progressively larger magnetic field values.

A simple phenomenological model for the field dependence of the strain was proposed by O'Handley et al. [22] and Murray [8]

$$\epsilon(H) = \epsilon_0 f = \frac{2K_u h(1 - h/2) - \sigma\epsilon_0}{C_{eff}\epsilon_0} \tag{1.2}$$

to interpret the results. In Eqn. 1.2, C_{eff} is the effective elastic modulus of the twinned state, f is the volume fraction of the variant with its c-axis parallel to the magnetic field, h is the reduced field (H/H_a), ϵ_0 is the peak strain, and K_u is the magnetocrystalline anisotropy energy. The coercivity is introduced into the model by expressing the external field as $H \pm H_c$ for decreasing or increasing field strength.

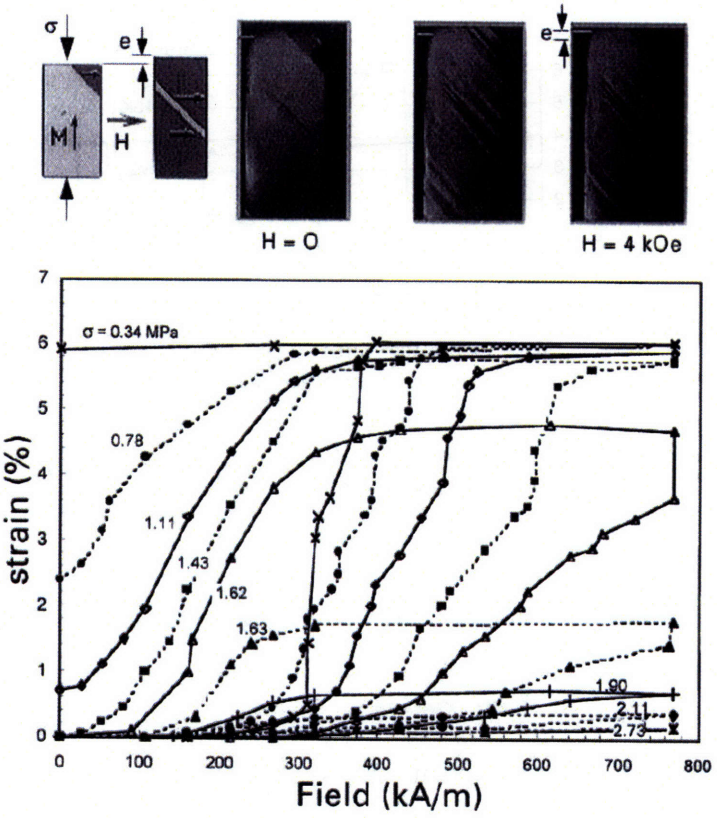

Figure 1-10: The ϵ-H response for a single crystal Ni–Mn–Ga specimen under 0.34–2.73 MPa applied loads. At the top right are 3 high-speed video frames showing the motion of twin-boundaries during the application of the magnetic field [21].

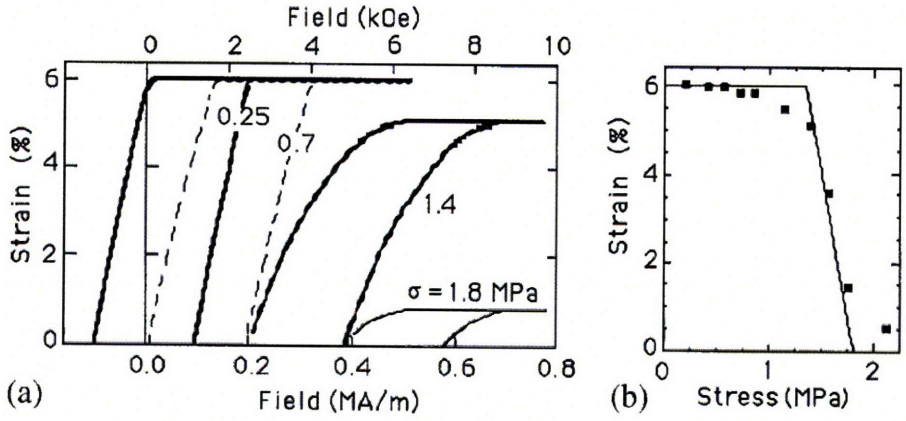

Figure 1-11: Calculated strain vs. applied field curves (a) from Eqn. 1.2 and the calculated strain vs. stress behavior overlaid with experimental data [21].

The model (Eqn. 1.2) gives a reasonable reproduction of the data. It correctly captures the increase in threshold and decrease in strain with applied load.

1.4.2 AC-strain response

The work of Murray was expanded on by Henry [23, 24, 25, 26] to include AC-performance. Henry used an experimental apparatus that incorporated a spring load applied to the end of the FSMA to provide the restoring force after FSMA extension. The magnetic field was then applied perpendicular to this load path and the magnetic field frequency could be varied to cause up to 500 Hz actuation.

The stress dependence observed by Henry [25] was similar to that initially observed by Murray [27]. For low values of the bias stress, the FSMA is not fully reset following MFIS and the cyclic strain is low (Figure 1-12). The largest values of stress, 2.18 MPa, are sufficiently large that the magnetic field is not capable of supplying sufficient energy to overcome the applied strain energy. At intermediate bias stress values of 1.41 MPa, cyclic strain is maximized as the bias stress is capable of resetting the crystal to its initially compressed condition, while not being large enough to block twin-boundary motion.

Henry also showed that Ni–Mn–Ga is capable of showing large cyclic strain at frequencies out to 500 Hz. Figure 1-13 shows some of the data for frequencies out to 100 Hz. Strain magnitudes remain nearly constant over this frequency range. A phase lag between the magnetic field and the strain response can be seen in Henry's data as an increase in the intercept of the data with the strain axis as the frequency is increased.

1.5 Magnet Design

The choice of magnetic circuit design is important to determine the size and power requirements for an actuator design. For Ni–Mn–Ga, the majority of the weight of the actuator is the magnet itself. The magnetic core and wire windings can account for over 95% of the total mass of the final actuator [15]. As a result, the reduction in

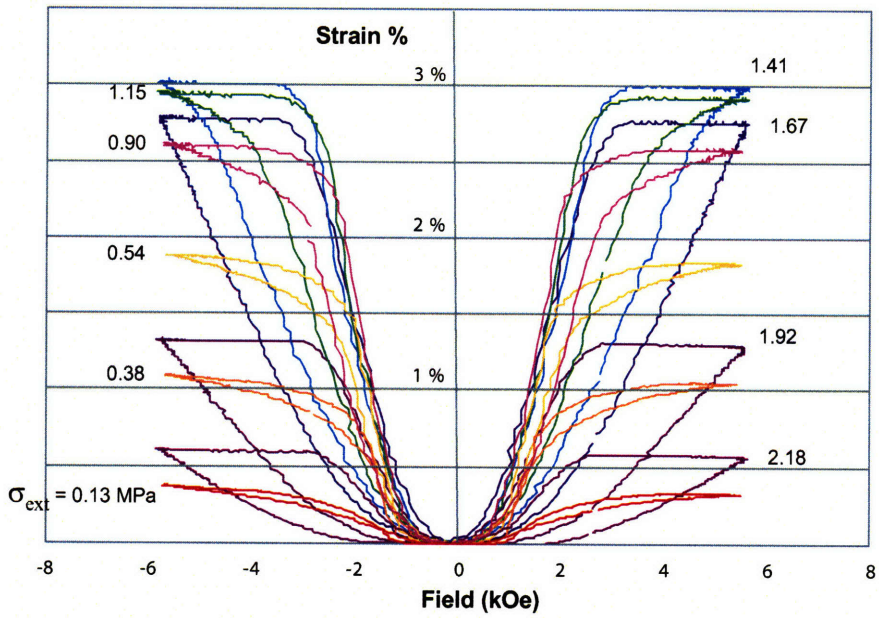

Figure 1-12: Strain vs. Magnetic field data for measurements taken at various bias stresses for 1 Hz actuation frequency [25].

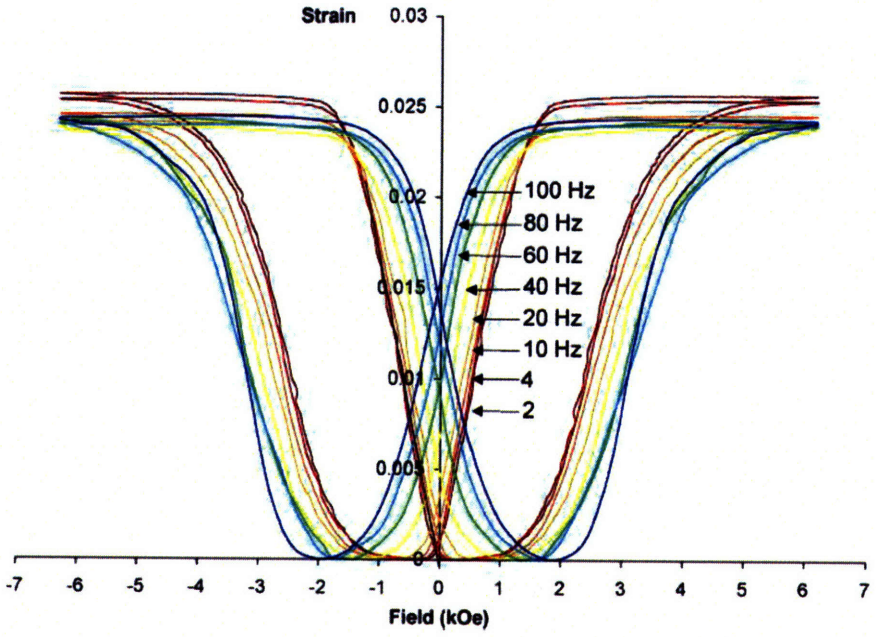

Figure 1-13: Strain vs. Magnetic field data for data taken at 1-100 Hz actuation with a 1.7 MPa bias stress [25].

magnet requirements are of utmost importance in the design of an FSMA actuator.

The magnetic field produced from an electrical current can be expressed as

$$NI = \oint H \cdot dl = \oint \frac{\Phi}{\mu A} dl \tag{1.3}$$

where N is the number of turns on the magnet, I is the current, Φ is the magnetic flux, μ is the permeability, dl is a differential length element along the magnetic circuit, and A is the cross-sectional area. For a single-component magnetic circuit,

$$NI = \frac{\Phi l}{\mu A} \tag{1.4}$$

For multi-component magnetic circuits, Eqn. 1.4 can be generalized as a sum over all the components such that

$$NI = \Phi \sum_i \frac{l_i}{\mu_i A_i} \tag{1.5}$$

From Eqn. 1.5, it can be seen that the magnetic flux, Φ, is directly proportional to the current, I, and the number of turns, N [1]. If the required field is reduced, the product of NI can be reduced by the same amount, assuming the gap size remains constant. If the drive current, I, is held constant, then the number of turns can be reduced thereby reducing the magnet size and weight as the magnetic field requirements are lowered.

The minimum electrical power needed to drive a magnet can be given as

$$P = VI = RI^2 \tag{1.6}$$

$$P = R\Big(\frac{\Phi}{N} \sum_i \frac{l_i}{\mu_i A_i}\Big)^2 \tag{1.7}$$

where V is the drive voltage and R is the resistance from the windings. The power is proportional to the square of the magnetic flux, Φ^2, so that any reduction in required magnetic field will result in a large reduction in power consumption.

[1] The linear relationship is valid for magnetic fields that are insufficient to saturate the core. For magnetic fields approaching the saturation field of the core, the relation between NI and Φ becomes non-linear.

For most magnet designs, the behavior of the magnet is governed primarily by the length of the air gap because the relative permeability of a magnetically soft core can be orders of magnitude greater than air ($\frac{\mu_{core}}{\mu_{air}} \approx 10^2$ to 10^4) [16]. The magnetic core materials are selected to maximize this ratio and the soft magnetic core is essentially lossless relative to the air gap as a result, allowing Eqn. 1.7 to be summed over the gap dimensions only. The electrical resistance of the magnet windings can be given as

$$R = \frac{\rho L}{A_w} \tag{1.8}$$

$$R = \frac{2\pi r N \rho}{A_w} \tag{1.9}$$

where ρ is the resistivity of the wire material, L is the total length of wire, r is the radius of the windings about the magnet core, and A_w is the cross-sectional area of the wire. Substituting Eqn. 1.9 into Eqn. 1.7 yields

$$P = \frac{2\pi r \rho}{N A_w}\left(H l_g\right)^2 \tag{1.10}$$

in which l_g is the length of the gap. It can be seen from Eqn. 1.10 that the DC power is inversely proportional to N and scales by the square of the magnetic field, H. Therefore, reductions in the magnetic field requirements can yield large power savings.

The operation of the magnet under AC conditions requires additional considerations. The flow of AC current in an inductor causes the formation of a back emf, called inductive reactance, that opposes the flow of charge as the frequency is increased. The inductive reactance as a function of the inductance, L, is given as

$$X_L = 2\pi f L \tag{1.11}$$

where L is the inductance in Henrys and f is the operating frequency in Hz. The

inductance for a solenoid is given by

$$L = \frac{\mu_0 \mu_r N^2 A_s}{l} \tag{1.12}$$

in which $\mu_0\mu_r$ is the permeability of the core material and A_s is the cross-sectional area of the solenoid. The net effect of the increase in reactance with frequency is a reduction in current flow through the magnet and a reduction in magnetic field at higher frequencies. To minimize the loss in current and achieve large magnet bandwidth, the inductance of the magnet can be minimized by reducing the number of turns, N, in the magnet and a laminated core material can be used.

1.6 Piezoelectric Materials

Piezoelectric ceramics are a class of electrically active materials. When an external electric field is applied to an unconstrained piezoelectric material, the material strains. The strains are typically small, <0.19% [28], and are fully reversible.

The piezoelectric effect can exist in materials that have non-centrosymmetric crystal structures. This accounts for 21 of the 32 space groups, 20 of which are piezoelectric[2]. An external electric field causes small displacements of the charged atoms within the unit cell and this displacement leads to the observed strain. The electric-field-induced strain can be expressed mathematically by

$$\epsilon_{jk} = d_{ijk} E_i \tag{1.13}$$

in which d_{ijk} are the piezoelectric moduli and E_i is the applied electric field vector [30]. It can be seen from Eqn. 1.13, that the strain is related to the magnitude of the applied field.

Piezoelectric materials are traditionally made from sintered solid particles from their individual oxide components. However, they can also be manufactured by chemical coprecipitation [31, 32] or hydrothermal techniques [33]. Once the starting ma-

[2]Space group 432 is not due to the other combined symmetry elements [29].

terial has been made, it is ball milled to improve homogeneity and then dried and mixed. The powder is then formed into shape by cold pressing, extrusion, slip casting, or other technique. The shaped compact then undergoes densification by sintering or hot pressing. Typical sintering conditions for PZT (lead zirconate titanate) are 1250 °C for 5 h in a flowing, oxygen-rich atmosphere. The domains within the polycrystalline structure are electrically aligned, or poled, by an external electric field so that the direction of strain in the grains is co-linear, producing a final polycrystalline material that behaves much like a single crystal. In the absence of poling, the sintered grains are randomly oriented and, on the whole, cancel each other out [29].

In the last several decades, PZT and PLZT (lead lanthanum zirconate titanate) have become common for transducer applications and have supplanted the traditional $BaTiO_3$ [29]. This is a result of the higher electromechanical coupling coefficient compared to $BaTiO_3$, higher operating ranges, easy poling, and ease of sintering relative to $BaTiO_3$.

1.6.1 Piezoelectric stack actuators

As a result of the low strain amplitudes (10s of nm) from a single layer of piezoelectric material, layers of piezoelectric ceramics are often assembled into a composite stack configuration. The individual piezoelectric plates are interdigitated with metal electrodes and co-fired into a solid, composite stack. This arrangement allows for a larger strain amplitude (1–10s of μm are readily achievable) at drive voltages <100 V. Additionally, larger energies can be applied to the load as a result of the larger displacements. However, larger currents are required to drive the stack devices due to their increased capacitance relative to a single layer. Figure 1-14 shows the displacement of a PZT stack actuator manufactured by Piezo Systems, Inc. which delivers up to 15 μm displacement at 90 V.

1.7 Motivation

It has been observed that there is a large variability in the properties of Ni–Mn–Ga with small changes in composition and crystal preparation techniques. The threshold field can vary by a factor of 2 with changes in composition of less than 0.5%, as is the case with data presented later in this thesis.

To date, it has been difficult to produce high yields of high-quality single-crystal material in this ternary alloy system. Despite the relatively low cost of the starting materials compared to those used in other magneto-active materials, the cost of growing high-quality single crystals of Ni–Mn–Ga remains high due to slow growth rate, difficulty in controlling the single crystal orientation, compositional control during the entire solidification process, and difficulty in controlling impurity levels. These high costs currently make Ni–Mn–Ga less attractive for commercial applications and have limited its applications.

Early data [35] showed that the application of a small amplitude acoustic drive with a piezoelectric was capable of reducing the threshold for the initiation of magnetic-field-induced strain in Ni–Mn–Ga and increases the overall FSMA strain output. The research was motivated by a desire to explore the range over which this effect on the threshold and strain could be observed and the limitations of the piezoelectric drive.

This ability to change the actuation characteristics of the material showed promise as a means of compensating for the variations in material properties that arise during processing. Lower quality materials with high defect concentrations could potentially be used with performance characteristics similar to higher quality crystals. The requirements on the material could be broadened, resulting in an overall decrease in production costs.

1.8 Thesis Layout

Chapter 2 addresses the role of defects on the actuation behavior and mobility of twin-boundaries. The first part of the chapter presents two models for twin-boundary

motion in the presence of defects. The second part of Chapter 2 presents data showing the strength and nature of defects that have been observed in single-crystal samples similar to those used in this thesis work.

Chapter 3 describes the crystal preparation and heat treatment used to produce the active FSMA crystals. The various experimental apparatuses that were constructed and used throughout this thesis work are also described.

Chapter 4 presents actuation data taken on samples from two different FSMA starting materials, TL7 and TL8, at 1 Hz actuation frequencies. The effect of the piezoelectric drive parameters on the strain and threshold are shown for magnetic field drive magnitudes near threshold and near saturation. The change in FSMA efficiency with the inclusion of the piezoelectric drive is also presented and indicates that the mechanical work done by the piezoelectric is a small fraction of the magnetic energy input.

Finite element modeling (FEM), shown in Chapter 5, is used to determine the resonant modes of the $X4$ experimental apparatus. The modeling results indicate that the compression spring used in the original apparatus design have numerous low-frequency resonant modes. Further FEM modeling was used to redesign the $X4$ apparatus and remove most of the low-frequency resonant modes.

Chapter 6 presents data taken on the redesigned $X4$ apparatus at actuation frequencies up to 500 Hz. The data indicate that the piezoelectric drive is most effective at low-frequencies and is overshadowed by system behavior at higher frequencies.

The temperature dependence on the efficacy of the piezoelectric drive is shown in Chapter 7. The acoustic drive has allows for increased strain output at lower temperatures and is most effective near the temperature threshold for FSMA magnetic-field-induced strain.

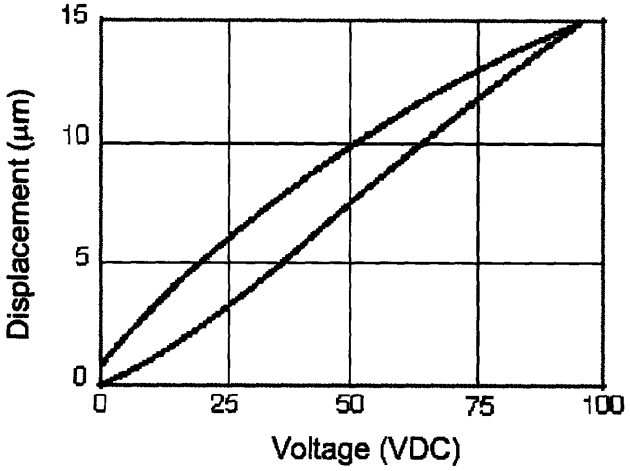

Figure 1-14: Free displacement of a PZT piezoelectric stack actuator measuring 5 × 5 × 18 mm [34].

Chapter 2

Theory of Actuation and Defect Interaction

In order to understand the effect of the piezoelectric drive, it is important to address the theory describing twin-boundary motion within the FSMA. In this chapter, models for the motion of twin-boundaries and their interaction with the lattice will be explored as well as the role of defects in the process.

2.1 Twin-boundary Models

Figure 2-1 shows the atomic positions of the atoms in two twin-boundary variants. In order for the twin-boundary to advance normal to its surface, the atom in position #1 must translate parallel to the twin-boundary into position #2. After all of the atoms on the boundary have undergone this translation, the twin-boundary will have advanced in the [101] direction by one atomic layer. In order for the atom to translate, it requires sufficient energy to overcome the energy barrier separating position #1 and #2. This energy barrier is typically modeled as a double-well potential [36] with the energy barrier given by $\Delta G_{activation}$. The energy barrier in a perfect crystal has the height of the Peierls potential. In a real crystal the energy barrier can be much greater due the presence of various material defects. Thermal energy ($kT \approx 25$ meV/atom) provides much of the energy to overcome the barrier, because twin-boundary motion

is suppressed at reduced temperatures [37]. An applied stress or magnetic field acts as a bias to reduce the energy of one position/variant over the other as shown in Figure 1-5. The bias energy from the magnetic field is on the order of 10 μeV/atom.

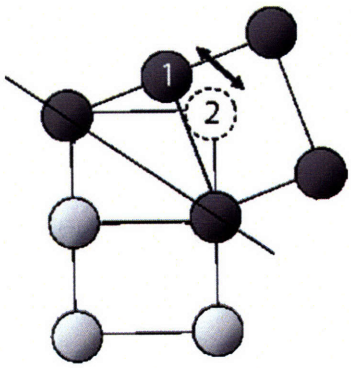

Figure 2-1: Geometry of the atomic positions at the twin boundary. In order for the twin boundary to advance vertically, the atom in position #1 must shear relative to the twin-boundary into position #2.

The energy difference between the two variants provides the driving force for twin-boundary motion. However, the mechanics of motion of the twin-boundary are governed by the local defect structure in the material.

Paul [38, 39] examines the interaction of a twin-boundary and a magnetic domain wall with a generic Gaussian defect. The model used

$$E = \int_{-D}^{X_A} \Big(A(\theta')^2 + K\sin^2(\Theta_1 - \theta) - HM\cos(\Theta_1 - \theta) + \epsilon^2 g(X, X_d) \Big) dx + \int_{X_A}^{D} \Big(A(\theta')^2 + K\sin^2(\Theta_2 - \theta) - HM\cos(\Theta_2 - \theta) \Big) dx \tag{2.1}$$

is an energy minimization formulation that accounts for magnetic anisotropy energy ($K\sin^2(\Theta_i - \theta)$), Zeeman energy ($HM\cos(\Theta_i - \theta)$), and exchange energy ($A(\theta)^2$) in each of the two variants and the strain energy from the elastic defect in magnetically preferred variant ($\epsilon^2 g(X, X_d)$). The preferred easy magnetization directions in variant #1 and #2 are given by Θ_i and the angle of magnetization is given by θ. The magnetization is taken such that in variant #1, $\theta_1 = 45°$ and $\theta_2 = 135°$ for variant #2 and θ is allowed to vary continuously across the domain wall. The model assumes a functional dependence on the x-coordinate only, thereby simplifying the resulting

calculations.

Paul finds that when the twin-boundary encounters a defect, the domain wall tends to lead the twin-boundary. As long as the strength of the defect is less than the anisotropy energy, the twin-boundary is capable of overcoming the defect with the application of a magnetic field of appropriate magnitude.

The strength of the defect has a strong impact on the magnitude of the magnetic field that must be applied to overcome any defects. This is clear because of the large magnitude of the thermal energy relative to the Peierls potential. For defect strengths greater than the anisotropy energy, the domain wall will break free of the twin-boundary and sweep through the entire length of the crystal and the twin-boundary will remain pinned at the defect. In this situation, the magnetic energy is insufficient to overcome the defect and twin-boundary motion is effectively blocked at the location of the defect [38]. Although one cannot make the simple assertion that the threshold required to initiate twin-boundary motion is the sole result of defects, it is clear that the presence of large, frequent defects will cause a larger threshold than would otherwise be observed.

Paul [39] also looks at the time-dependent solution of the motion of a partial dislocation along the twin-boundary in the presence of an elastic defect. The partial represents the leading edge of the atoms adjacent to the twin-boundary plane that have transformed from the original variant into another variant. Once the partial dislocation has swept the length of the twin-boundary (see Figure 2-1), the twin-boundary advances one atomic step normal to its plane (in the [101] direction). The model is formulated in terms of an unperturbed Lagrangian such that

$$L_u = \sum \left(\sigma_s(T) \left[\frac{2U_i^2}{\mu^2} - \frac{U_i^4}{\mu^4} \right] - A_{ex} \left(\frac{dU_i}{dx} \right)^2 + \frac{m}{2} \left(\frac{dU_i}{dt} \right)^2 \right) \tag{2.2}$$

in which A_{ex} is the nearest neighbor exchange energy, μ is the atomic displacement of variant #2 from variant #1, $\sigma_s = 10^7 \text{dynes/cm}^2$ is the atomic stress magnitude with respect to the lattice, U_i is the time-dependent displacement of the atoms along the twin-boundary in the x-direction. The energy barrier for the double well is at least

that of the Peierls potential and can be strongly modified by local material defects.

It is found that the interaction of the defect's strain field with the twin-boundary will cause a deceleration of the twin-boundary as it nears the repulsive defect and impedes its motion [39]. Once the dislocation at the twin-boundary interface passes the defect, it is accelerated away from the defect as a result of the defect's repulsive strain field. The acceleration persists until the partial dislocation reaches the initial velocity profile that it would have been on had it not encountered a defect (Figure 2-2). The net result of elastic defects is therefore that the average twin-boundary velocity is reduced.

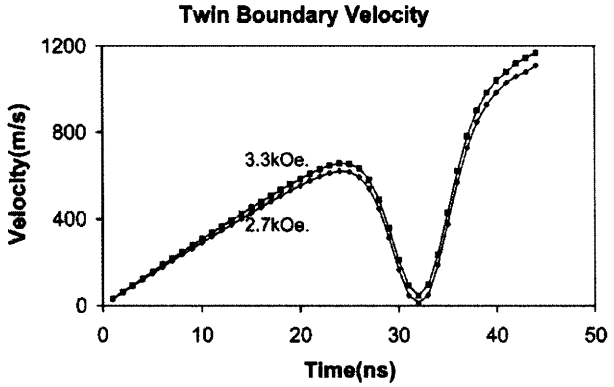

Figure 2-2: Velocity of a partial dislocation moving along a twin boundary in the presence of a defect. The partial dislocation is decelerated as it approaches the defect, and accelerated as it passes the defect [39].

Paul's model also explains why the FSMA crystals do not extend at the speed of sound. Extension of the crystal requires that a partial dislocation moves across the width of the crystal to cause an elongation along the length of the crystal equal to one atomic layer in the [101] direction. These partial dislocations may move at speeds approaching the sound velocity, however the large distances that they must move precludes the rapid elongation of the FSMA crystal.

Using the same model with the inclusion of a weak acoustic-drive (piezoelectric drive), Paul finds that the addition of the weak acoustic perturbation results in the reduction in magnetic threshold for the motion of a dislocation past a given defect strength (Figure 2-3). The reduction in threshold is increased for both increasing

acoustic frequency and amplitude. Quantitative comparisons with experimental data are difficult however, as it is non-trivial to relate the macroscopic piezoelectric displacements to atomic displacements along the twin-boundary.

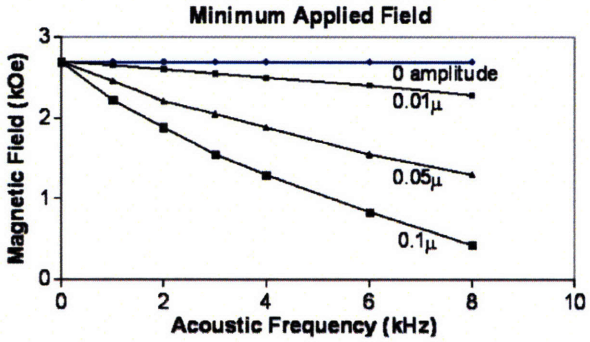

Figure 2-3: Modeling results of the effect of a small amplitude acoustic drive on the threshold magnetic field required to overcome a defect. The various curves are for different amplitude acoustic drives [39].

An alternative model based on the torque on the twin-variants has been proposed by O'Handley [37]. The magnetic-field-induced torque is defined as

$$\Lambda = \frac{-\partial G_{Zeeman}}{\partial \theta} \tag{2.3}$$

and the magnetic-field-dependent torque per unit volume is given by

$$\lambda = \frac{\Lambda}{\Omega} = -\frac{\partial(-M_s H \cos\theta_2)}{\partial \theta} = -2K_u h\sqrt{1-h^2} \tag{2.4}$$

in which h is the reduced magnetic field, M_s is the saturation magnetization, and θ_2 is the angle of the magnetization vector from the easy axis. In an unconstrained case, the crystal would rotate such that the net moment aligns parallel to the field. However, the external constraints prevent crystal rotation and provide the opposing force. The torque results in only the motion of atoms in variant #2 in Figure 2-4 and this motion proceeds in a wave-type fashion along the twin-boundary. The temperature dependence of the torque is expressed using the relation derived by

Callen and Callen [40]

$$K_u(T) = K_u(0)m^2 = K_u(0)\left(1 - \left(\frac{T}{T_c}\right)^2\right)^2 \tag{2.5}$$

where T_c is the Curie temperature and m is the reduced magnetization. Including Eqn. 2.5 in Eqn. 2.4, yields the temperature dependence of the magnetic torque

$$\lambda(T) = -2K_u(0)h(T)\sqrt{(1-t^2)^2 - h(T)^2} \tag{2.6}$$

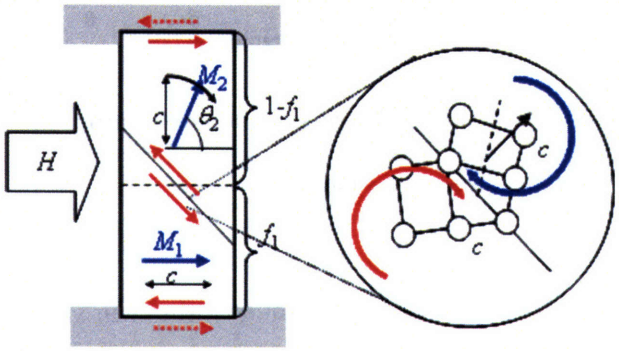

Figure 2-4: Diagram of the forces and torques on the FSMA single crystal in a magnetic field. The volume fraction of variant #1 is given by f[37].

O'Handley also looks at the temperature dependence of the magnetic-field-induced shear stress (10 μeV/atom) relative to the thermal energy (≈25 meV/atom). A thermally activated process is modeled by the standard exponential

$$R_i = R_0 \exp\left(-\frac{\Delta G_i}{k_b T}\right) \tag{2.7}$$

where R_0 is the pre-exponential factor, k_b is the Boltzmann constant, and ΔG_i is the barrier height between variant 1 or 2. The energy barrier as in Paul's model can vary widely as the result defects and in general is approximately 1000 times larger than the magnetic energies.

Given Eqn. 2.7, the probability of a twin-boundary moving can be expressed as a

difference in the rate of transition between the two states of the double well potential:

$$R_{2\to 1} = R_0 \left[\exp\left(-\frac{\Delta G - G_{mag2}}{k_b T} \right) - \exp\left(-\frac{\Delta G - G_{mag1}}{k_b T} \right) \right] \tag{2.8}$$

where G_{magi} can be found from Eqn. 2.6. Then, the condition for magnetic-field-induced twin-boundary motion is

$$\lambda_{101}(T) R_{2\to 1}(T) > \tau_y(T) \tag{2.9}$$

in which τ_y is the twin-boundary yield stress. Figure 2-5 shows the temperature dependence of the magnetic torque, in terms of the pre-exponential factor. Two forms of the twin-boundary yield stress are shown, one linear in temperature and the other exponential, based on Heczko's measurements [20]. At low temperatures, the lack of thermal energy freezes out the transition between double-well minima. The magnetic torque is a maximum for reduced temperatures in the range 0.6–0.7. For these temperature values, the anisotropy energy and the thermal energy are large. On approaching the Curie temperature, $t = 1$,

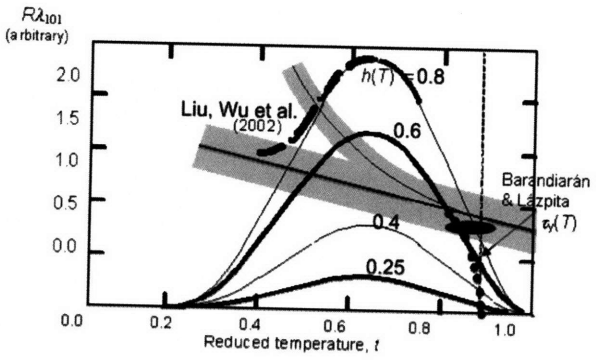

Figure 2-5: Schematic of the magnetic torque as a function of the reduced temperature [37]. The dashed line represents data from Lu [41].

2.2 Material Defects

Experience indicates that defects play a significant role in the mobility of twin-boundaries in Ni–Mn–Ga as crystals of similar composition can have widely varying actuation properties. The models reviewed above attempt to take this into account in slightly different ways. To date, little work has been done on determining the exact nature of the defects or their strength. Marioni [11] reported the defect strength distribution for a single crystal based on the onset of twin-boundary motion, measured optically, under the application of successively stronger pulsed magnetic fields. He found a distribution of defect strengths, with a large concentration of defects with energies of 0.56 K_u spaced throughout the crystal length [42]. Defects stronger than K_u could not be quantified by his experimental method.

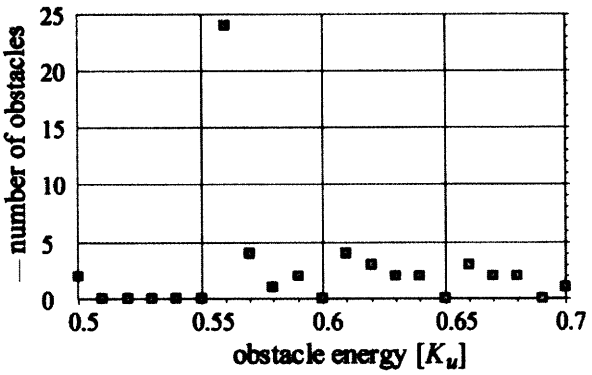

Figure 2-6: Defect strengths measured by Marioni in a single crystal of Ni–Mn–Ga [11].

Through transmission electron microscopy (TEM) observation of the microstructural characteristics of single crystal Ni–Mn–Ga samples, Richard [43] determined the concentration, size, and composition of second phase defects. Both Ti-rich and S-rich phases were found throughout the samples tested. The Ti-rich second phase particles were coherent, as evident from the Ashby-Brown strain contrast in Figure 2-7, and are on the order of 5–20 nm in diameter. These inclusions tended to appear in clusters and were noted to align into chains in some instances.

The S-rich phases were larger in size (100–1000 nm), and are incoherent. It was

found that magnetic-field-induced strain (MFIS) was not observed in samples cut from single crystal boules that had a large concentration of sulfur inclusions while those with low concentrations did show magnetic-field-induced strain. A simple Orowan model for the stress required for dislocation looping past the second phase inclusions

$$\tau = \frac{Gb\sqrt{f}}{r} \tag{2.10}$$

was used to estimate the strength of the defects. Here G is the the shear modulus, b is the Burgers vector, f is the inclusion volume fraction, τ is the required stress, and r is the mean radius of an inclusion [43]. Richard's results are summarized in Table 2.1. The model predicts correctly that the samples with large concentrations of S inclusions do not show strain. The results for the low concentration samples are also consistent with the defect strengths measured in an active crystal by Marioni [11].

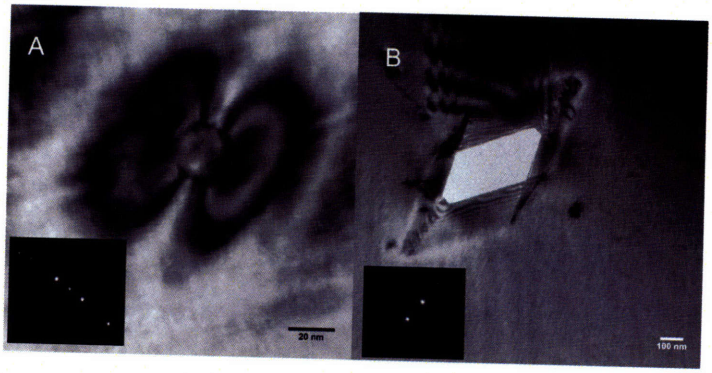

Figure 2-7: Two second-phase defects that have been found, using bright-field imagining, in samples similar to those used in this thesis. A shows a coherent Ti-rich phase approximately 20 nm in diameter and B shows a S-rich, incoherent particle approximately 200 nm in diameter which runs through the width of the specimen. Both second phase particles are crystalline, indicated by the inset selected area X-ray diffraction patterns [43].

Impurity	r (nm)	Approximate f	Calculated Strength (K_u)	MFIS
S in TL5	500	0.01	1.58	No
S in TL8	500	0.001	0.50	Yes

Table 2.1: Estimated defect strength of S inclusions using a dislocation looping model and whether the samples showed magnetic-field-induced strain (MFIS) [43].

Chapter 3

Methodology & Experimental Setup

3.1 FSMA Preparation

Oriented single crystals of Ni–Mn–Ga were grown by the Bridgeman method [44] at Ames National Laboraties in Ames, Iowa. The received crystal boules were approximately 25 mm diameter and 75 mm long. Rectangular prisms having faces parallel to the parent {100} planes and measuring approximately $2.5 \times 2.5 \times 15$ or $2.5 \times 4 \times 15$ mm were cut from the starting material at MIT using a Charmilles Robofil 240cc wire EDM. These were then lightly polished down to 4000 grit paper and encapsulated in quartz ampules under argon atmosphere. In addition, tantalum turnings were included in the ampules as an oxygen scavenger, to further prevent surface oxidation during heat treatment.

Heat treatment was performed by holding the crystals at 850 °C for 24 hours then slowly cooling to 500 °C and holding for 2 hours to allow for $L2_1$ ordering. They were then cooled to 200 °C and held at that temperature until removal from the furnace. The final cool down to room temperature was performed with the crystals under a constant compressive load of approximately 10 MPa, along the long axis of the crystal, to facilitate formation of a single-variant state with the c-axis oriented along the direction of the compressive load.

Single crystal specimens were cut from two single crystal boules, labeled TL7 and TL8. The nominal compositions are presented in Table 3.1. The composition of TL8 is consistent throughout its length, however TL7 has a more substantial composition gradient. Figure 3-1 shows the composition of TL7 and TL8 relative to other compositions that have been identified. Both samples have similar transformation temperatures (shown by the solid lines) and have shown magnetic-field-induced strain.

Crystal	Ni	Mn	Ga
TL7	50.7	27.7	21.6
TL8	50.3	28.2	21.5

Table 3.1: Nominal compositions (at%) of the crystal boules from which the samples used in this thesis were taken.

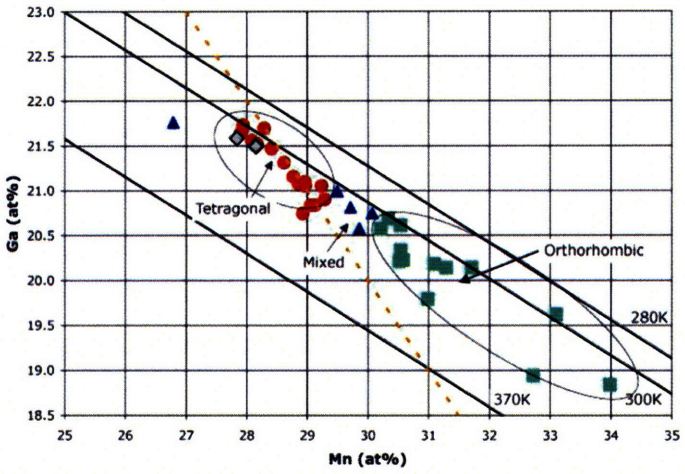

Figure 3-1: Composition map for Ni-Mn-Ga. The dotted line represents the 50% Ni compositions and the solid lines represent martensite transformation temperatures. Red circles are compositions that have been identified as tetragonal, green squares are orthorhombic compositions, and blue triangles are compositions that contain mixed martensitic phases [43, 45]. TL7 and TL8 are identified on the figure with grey diamonds.

3.2 Actuators

3.2.1 Low-Frequency $X1$ Magnet

In order to measure the effect of the piezoelectrically supplied acoustic energy, three different assemblies were used. The first of these was based on the $X1$ magnet used by C.P. Henry [25]. The $X1$ is a large inductance magnet, which when driven with low drive current, is suitable for producing large magnetic fields at frequencies near 1 Hz (Table 3.2).

Single-crystal specimens of Ni–Mn–Ga are oriented in the magnet with the long direction (c-axis) perpendicular to the direction of the applied field. This allows for the crystal to expand against the load as the magnetic field is increased and for a spring force, oriented along the long axis of the crystal, to reset it to the compressed state as the magnetic field is decreased to zero. A Piezo Systems, Inc. model TS18-H5-104 PZT (lead zirconium titanate) piezoelectric stack actuator is placed below the FSMA crystal and is held in place with 2-sided tape. Also located within this load path is a load cell with a 25 lb range (well in excess of 10 MPa for the sample dimensions used here) and a brass flexure for measuring displacement, see Figure 3-2. A pair of thin brass flexures are used to maintain the alignment of the parts in the load path, and also provide a portion of the restoring force on the FSMA. Strain is determined by measuring the displacement of the uppermost member that extends from the flexure and to the right in Figure 3-2 with an ADE model 3800 capacitance gauge. This configuration was used instead of earlier designs [25] as it has reduced losses from sliding friction because of the removal of moving pistons. These components are mounted on a rigid frame attached to the $X1$ electromagnet such that the magnetic flux is oriented perpendicular to the load path and the FSMA is in the center of the gap where the field is uniform.

This experimental apparatus was used for collection of low-actuation-frequency data near 1 Hz. The procedure used for data collection is outlined below:

1. The prestress applied to the FSMA by the spring was adjusted for maximum

strain output of the FSMA. Typically, this stress was near 1 MPa on the crystal.

2. The drive voltage and frequency for the piezoelectric were set to the desired values ranging between 0–20 kHz and 0–25 V_{rms} (See Figure 1-14 for corresponding piezoelectric displacement).

3. The drive voltage and frequency for the magnetic field were set for the desired value. For the $X1$ magnet, the drive frequency was limited to 0.5 Hz (1 Hz actuation).

4. The LabView electronic data collection software was initialized. The data collection was triggered by the magnetic field as the value rose from zero volts.

5. Once the data collection was completed, both the piezoelectric and magnetic field drive voltages were reset to zero.

Wire Gauge	18
Turns per coil	1000
Resistance in parallel	4.4 Ω
Inductance in parallel at 60 Hz	117.7 mH
Gap Volume	5.4 cm^3
Maximum Current	14 A
Maximum Field	9 kOe

Table 3.2: $X1$ magnet specifications [25]

3.2.2 High-Frequency Actuator

The second magnet, $X4$ (Figure 3-3), was a higher-frequency, low inductance design capable of delivering magnetic fields above the strain saturation field, for Ni–Mn–Ga, to 250 Hz (Figure 3-4). It also had differences in the components placed in the load path, which were primarily made out of steel in the $X4$ design, rather than aluminum (Figure 3-3). These modifications resulted in a 50% mass reduction of the moving parts compared to the $X1$ design, thereby increasing the resonant frequencies of these actuator components and producing better overall frequency response. As

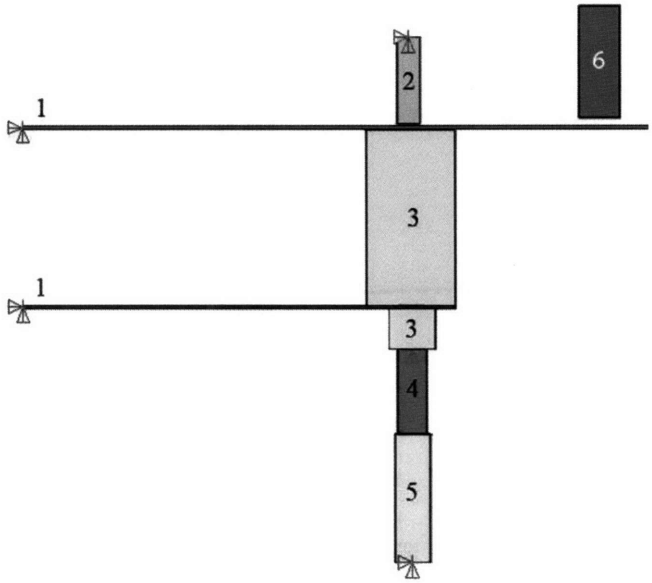

Figure 3-2: Schematic of the major $X1$ actuator components within the load path. The magnetic field is centered about the FSMA and oriented into the page. Material breakdown: 1.) brass 2.) spring 3.) aluminum 4.) FSMA crystal 5.) piezoelectric stack 6.) capacitance gauge.

in the $X1$ design, these components were mounted to a rigid frame attached to the electromagnet such that the magnetic flux is oriented perpendicular to the load path and centered on the FSMA crystal.

Wire Gauge	10
Turns per coil	140
Resistance in parallel	0.17 Ω
Inductance in parallel at 60 Hz	2.1 mH
Gap Volume	3.6 cm^3
Maximum Current	40 A
Maximum Field	9 kOe

Table 3.3: $X4$ magnet specifications [25]

For the high-frequency apparatus, special care had to be taken to match the spring stiffness to the test frequency and desired strain output from the FSMA. By equating the kinetic energy of the moving parts with the maximum magnetic energy input (Eqn. 3.1), the maximum actuation frequency of the FSMA can be determined. This

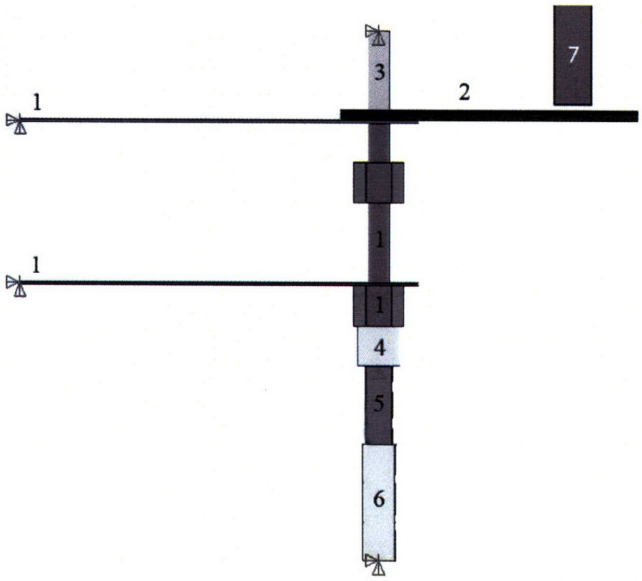

Figure 3-3: Schematic of the $X4$ actuator components within the load path. The magnetic field is centered on the FSMA and oriented into the plane of the page. Material Breakdown: (1) steel, (2) fiberglass composite, (3) spring, (4) aluminum, (5) FSMA, (6) piezoelectric stack, and (7) capacitance gauge.

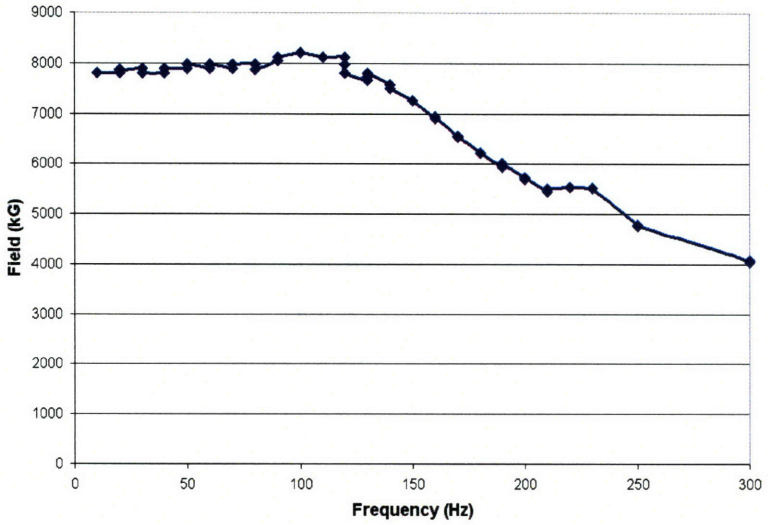

Figure 3-4: Magnetic field produced by the $X4$ magnet with a fixed drive voltage. Higher voltage drives can produce a maximum of approximately a 10 kOe field

analysis shows that a 2 cm Ni–Mn–Ga crystal is capable of actuation up to 850 Hz. Here it is assumed that the sample is not subjected to a bias stress and only the

sample moves.

$$\frac{1}{2}mv^2 = K_u V \tag{3.1}$$

$$v = \sqrt{\frac{2K_u}{\rho_m}} \tag{3.2}$$

$$\omega \Delta x = \sqrt{\frac{2K_u}{\rho_m}} \tag{3.3}$$

$$\omega \epsilon L = \sqrt{\frac{2K_u}{\rho_m}} \tag{3.4}$$

$$f = \frac{1}{2\pi\epsilon L}\sqrt{\frac{2K_u}{\rho_m}} \tag{3.5}$$

$$f = \frac{1}{2\pi(0.06)(0.02)}\sqrt{\frac{2(1.5 \times 10^5)}{8140}} \tag{3.6}$$

$$f = 850 \text{ Hz} \tag{3.7}$$

When a spring is present, one must also take into account the maximum rate that the spring can compress the FSMA crystal back to its original state. To find this rate, the resonant frequency of the spring must be found and is shown in Eqn. 3.8, assuming a moderate spring stiffness of 12 kN/m. This frequency comes out to be 123 Hz, well below the theoretical frequency at which the FSMA can actuate. Therefore, the resonant frequency of the spring (and the other mechanical components) is the controlling factor in the bandwidth of the device. This is discussed further in Chapter 5.2.

$$\omega = \sqrt{\frac{k}{m}} \tag{3.8}$$

$$\omega = \sqrt{\frac{12 \times 10^3}{0.02}} \tag{3.9}$$

$$f = \frac{\omega}{2\pi} = 123 \text{ Hz} \tag{3.10}$$

There is a tradeoff between bandwidth and displacement from the apparatus.

Stiffer springs allow for higher frequency actuation, but block twin boundary motion much earlier than do weak springs due to the larger stresses they apply to the crystal at a given strain. This also means that long crystals will inherently have a lower bandwidth in this type of device as they require more compliant springs for full 6% strain.

Once an appropriate design of the reset mechanism had been determined, data collection was carried out in the same manner as the $X1$ apparatus. The only significant difference was that the magnetic field was operated at various frequencies in a burst mode of 2–10 magnetic field cycles to limit undesirable heating of the magnet power supply. Otherwise, the experimental conditions and procedure were identical for the two apparatuses.

3.2.3 Temperature Dependence

The $X4$ apparatus was modified to allow for temperature dependent measurements of the effect of the piezoelectric drive on the FSMA. A styrofoam enclosure was placed around the entire $X4$ magnet assembly to provide for an insulated, temperature controlled environment. A thermocouple was placed adjacent to the FSMA crystal to monitor the ambient temperature. The temperatures below room temperature were achieved by the addition of a combination of dry ice and liquid nitrogen via an access port on the top of the enclosure. After the desired minimum temperature was achieved and stabilized for 10 minutes, the temperature was allowed to slowly rise as data points were collected. This temperature drift for the apparatus was less than 0.1 °C/min.

3.2.4 Adaptamat Actuators

In addition to the two test systems described above, two actuators from Adaptamat were used to test the effect of acoustic-assistance with a small, commercially-available device. Specifications for these devices are given in Table 3.4. The first of the two was left unaltered as a control specimen, as shown in Figure 3-5. The second actuator

Blocking force	approx. 25 N
Maximum operating frequency	500 Hz
MSM element dimensions	5 x (0.95 x 2.0 x 39) mm 38 mm active length
Actuator dimensions	40 x 40 x 67 mm (100 mm long with shaft)
Total mass	2 x 560 g
Maximum peak current	3.0 A in both coils
Turn number	2 x 108
Wire diameter (in/out)	0.71/0.77 mm
Time constant of winding	30 ms
Lamination Sheet thickness	0.2 mm
Lamination package thickness	39 mm

Table 3.4: Manufacturer specifications for the Adaptamat actuators

was modified to include a piezoelectric stack in series with the FSMA crystal so that the efficiency of the acoustic assistance could be determined, Figure 3-6.

Each Adaptamat actuator was fitted with a collet which held a capacitance gauge in place for displacement measurements. A 12.7 mm diameter aluminum target weighing 2.3 g was attached to the end of the actuator's shaft for use in conjunction with the capacitance gauge. This allowed for accurate displacement measurements to be made in reference to the actuator. The drive current to the devices was measured for the modified device, Adaptamat #2, as well as the piezoelectric drive voltage and frequency.

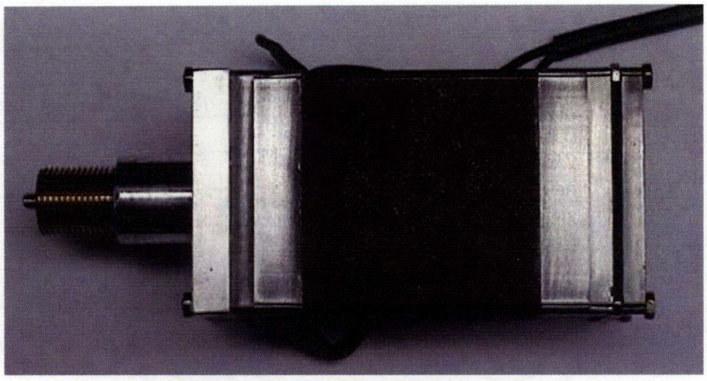

Figure 3-5: The Adaptamat #1 actuator showing the device in the as-received state.

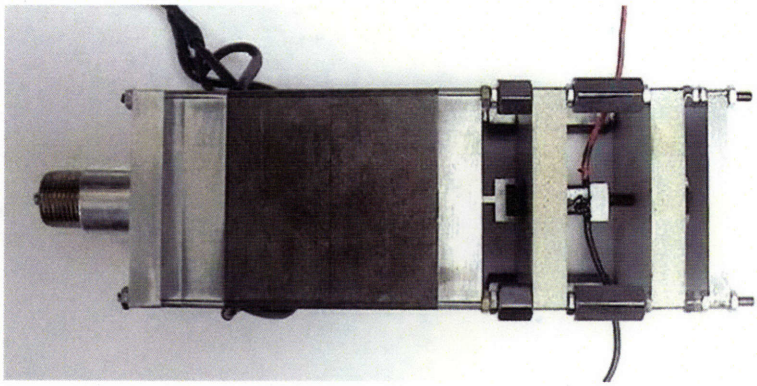

Figure 3-6: Adaptamat #2 showing modifications to allow for acoustic assist.

Chapter 4

Low-Frequency Actuation

This chapter describes the effect of acoustic waves on the low-frequency actuation (1 Hz magnetic drive) of Ni–Mn–Ga single crystals. The data were collected on the $X1$ experimental apparatus described previously in Chapter 3.2.1. Changes in threshold field, strain output, stress output and efficiency will be discussed.

4.1 ϵ vs. H Minor loops

The effectiveness of acoustic energy applied to a Ni–Mn–Ga crystal from TL7 during magnetic actuation is evident in a series of experiments measuring the FSMA strain output with a DC-biased magnetic field and a spring for for bias stress for crystal reset. In Figure 4-1, the FSMA begins in a compressed state and extends against the load after the magnitude of the magnetic field exceeds a threshold value. The FMSA continues to strain until it reaches its maximum value at the maximum magnetic field. As the field is reduced, the FSMA is compressed by the load to its original state. The piezoelectric stack was operated at 1 kHz with drive voltage of 5, 35, and 55 V_{pp} (corresponding to a piezoelectric free displacement of 0.75 μm, 5.5 μm, and 8.7 μm, respectively, Figure 1-14) and thereby creating different amplitude stress waves within the FSMA at the same 1 kHz frequency.

With an increase in acoustic input from 5 V_{pp} to 55 V_{pp}, the threshold magnetic field value is reduced and the overall cyclic strain is increased concurrently. The data

show a reduction in the threshold values by roughly 500 Oe and a near doubling of the output strain between the 5 and 55 V_{pp} piezoelectric drives.

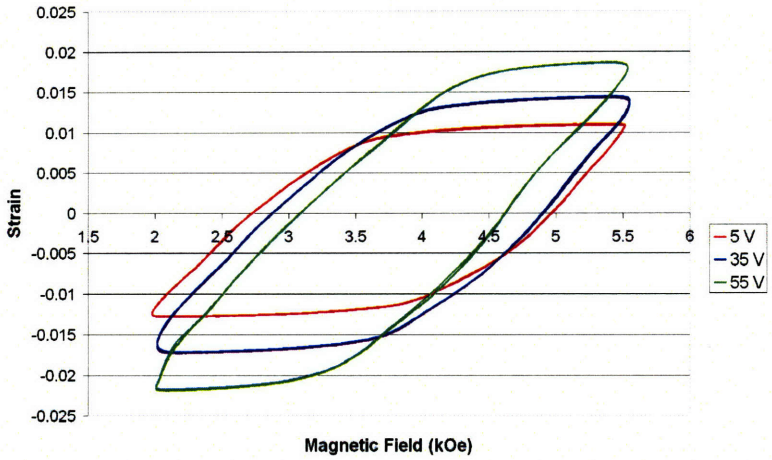

Figure 4-1: Early data showing the effect of acoustic-assistance. As the drive voltage for the piezoelectric stack is increased, the threshold for twin-boundary motion is reduced and the AC strain output increases [35].

Figure 4-2 shows the effect of varying the frequency of the piezoelectric. In this set of data, the magnetic field (-5100< H <4370 Oe) is offset slightly to negative field such that the maximum negative field is above the threshold. For the positive field side, the maximum field is below the threshold for twin-boundary motion when there is no acoustic input. As a result, there is very little AC strain for low acoustic frequencies (30 Hz) for H >0, as the field is insufficient to initiate twin-boundary motion.

As the acoustic frequency is increased, there is a reduction in the threshold magnetic field. As a result, there is a corresponding increase in strain output from the FSMA (Figure 4-3). For H <0, the output strain increases by 68% as the piezoelectric frequency goes from 30 Hz to 6 kHz. This effect is more pronounced for H >0 where an increase in strain output of 800%, relative to the initial strain, is achieved over the same piezoelectric frequency range. The more significant enhancement of piezo-assisted MFIS for $H > 0$ than $H < 0$ is due to the threshold being reduced to well below the applied magnetic field amplitude as the acoustic drive is increased,

allowing the magnetic field to cause actuation where it was previously incapable. Although the magnitude of the effect differs between $H < 0$ and $H > 0$, the addition of acoustic-assistance allows for the magnetic energy to be used more efficiently in both cases, as less is wasted in achieving the necessary threshold field and more of the energy is converted into useful work.

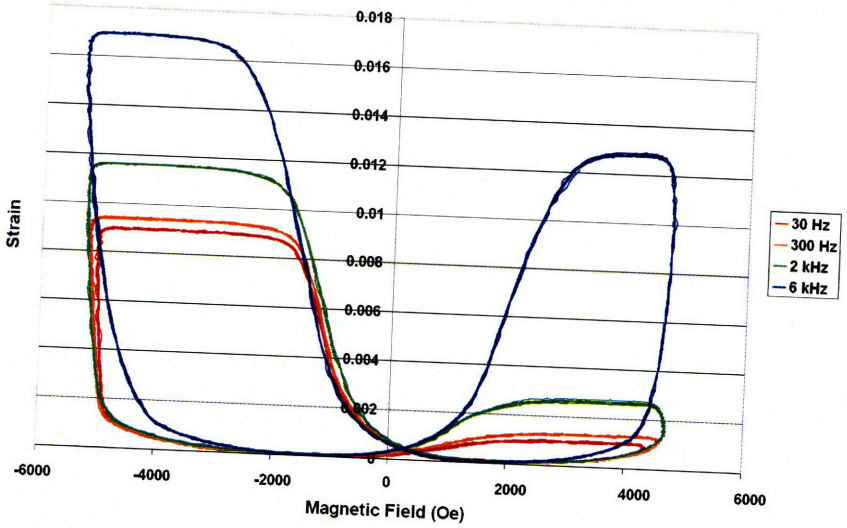

Figure 4-2: Strain-field butterfly curves at 1 Hz with varying frequency acoustic-assist. There is a small DC offset in the magnetic field such that for H <0, the maximum magnetic field is slightly greater than threshold and for H >0, the maximum field is below the threshold field. The strain increase is most pronounced for H >0 and the increase on each side is due to the reduction in threshold magnetic field. The red, green, and blue curves correspond to 30, 2000, and 6000 Hz respectively, at 20 V_{p-p} [35].

4.2 Large magnetic field drive

The previous section describes the effect of the acoustic drive on the FSMA when driven with a magnetic field lower than that required to saturate the FSMA strain. The following section will address the effects of the acoustic-assistance on the actuation behavior of the FSMA when it is driven by magnetic fields large to enough to cause magnetic saturation.

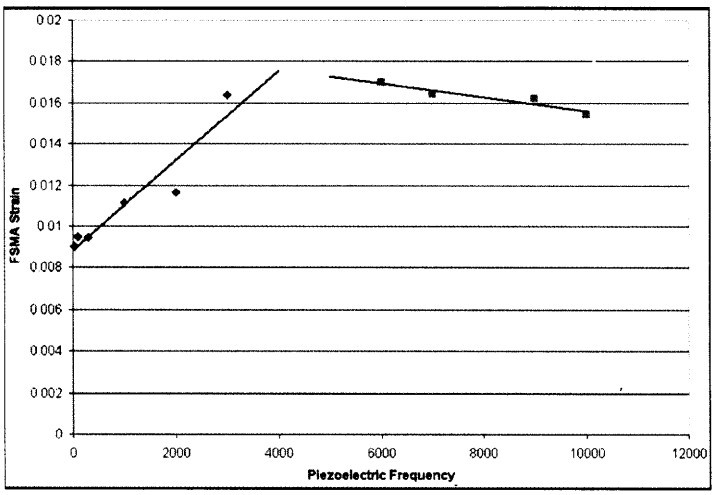

Figure 4-3: Comparison of the peak strain values in Figure 4-2 for H<0. Two regions of behavior are observed. There is an initial region in which strain increases rapidly to roughly 4.0 kHz, after which the strain output is roughly constant with a shallow decline up to 10.0 kHz [35].

Figure 4-4 shows the ϵ vs. H for a sample of Ni–Mn–Ga taken from crystal TL7. The FSMA was actuated with a sinusoidal magnetic field at 1 Hz with varying amounts of acoustic-assistance. The data shows that there is an initial magnetic threshold at H =4800 Oe and an initial cyclic strain of 3.28%. With the addition of a 20.3 V_{pp} acoustic drive at 5.0 kHz, the threshold is reduced by 1000 Oe (21%) to 3800 Oe. The FSMA strain at this acoustic frequency is increased to 3.46% strain. For a 10.0 kHz drive, the threshold is reduced slightly more than for the 5.0 kHz drive and the strain is equivalent at 3.46%. The strain increase with acoustic-assistance under large magnetic fields is substantially lower than what is observed when the FSMA is driven with a smaller magnitude magnetic field. The reason for this is three-fold. First, the maximum applied magnetic field is substantially above the threshold field and therefore the threshold is not directly controlling the overall strain, so that a reduction in the threshold has a small overall effect. Second, the Ni–Mn–Ga crystal has extended to near its theoretical maximum strain under an applied load prior to the addition of the acoustic-assistance, so the potential gains are smaller. This maximum

theoretical strain is given mathematically by [8]

$$\epsilon(\sigma, h) = \frac{2K_u h\left(1 - \frac{h}{2}\right) - \sigma\epsilon_0}{C\epsilon_0} \tag{4.1}$$

in which $K_u = 1.7 \times 10^5$ J/m^3 is the magneto-crystalline anisotropy, h is the reduced magnetic field, $\epsilon_0 = 0.06$ is the maximum strain, and $C = 2 \times 10^7$ N/m^2 is the effective stiffness during twin-boundary motion [21]. With a bias stress of 1 MPa, the maximum strain predicted is 4.16%, although this value is sensitive to the value of the magneto-crystalline anisotropy, K_u. Third, all of the test apparatuses used throughout this thesis work constrain the crystal on its upper and lower surfaces. These constraints prohibit twin-boundaries from passing through a triangular section (dark regions on Figure 4-5b) at the upper and lower surfaces of the crystal, because the surface kinks (red encircled region on Figure 4-5c) produced by the twin-boundaries on passing along the constrained surfaces cause unfavorable stress concentrations. This decreases the effective active length by the width of the crystal. Correcting for this inactive region gives strains of 3.94% and 4.15% for the experiment with and without-acoustic assistance, respectively, which coincide closely to the theoretical values for a bias stress of 1 MPa.

For the same experiment, stress data was also recorded (Figure 4-6) using a compression load cell. The change in stress is a result of the magnetic-field-induced expansion of the FSMA crystal against a bias spring. In these curves, the FSMA begins at zero strain and the stress and strain increase simultaneously along the upper section of the curve as the magnetic field is increased (toward B). The maximum in stress, strain, and field occur simultaneously after which the stress and strain fall off with decreasing magnetic field along the lower section of the curve (toward A). From this plot (Figure 4-6), it can be seen that the acoustic-assistance has little effect on the stress output of the FSMA as $\Delta\sigma$ is the same with or without the piezoelectric drive. As can be seen in Figure 4-4 as well, there is an absolute increase in strain output of 0.18% strain with the addition of acoustic-assistance.

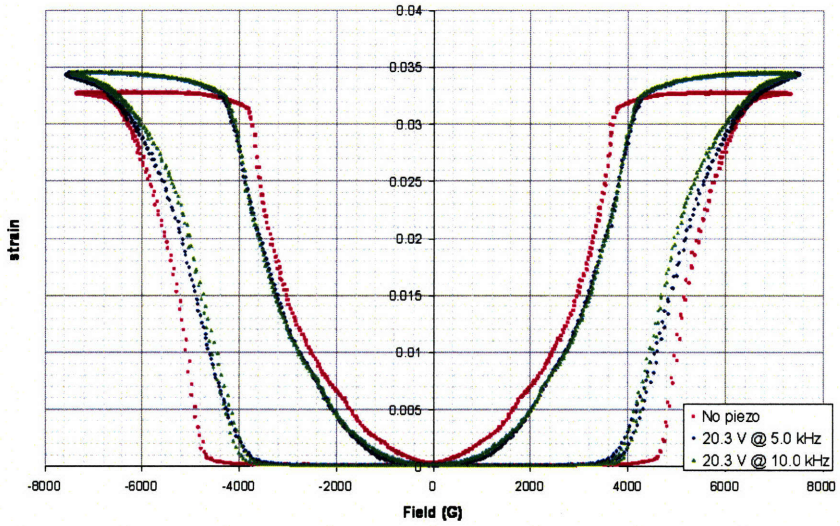

Figure 4-4: Effect of acoustic-assistance on the ϵ vs. H behavior for a large magnetic field drive.

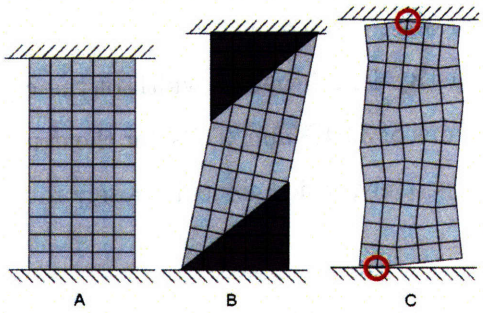

Figure 4-5: Schematic of single crystal of Ni–Mn–Ga at differing twin states. (A) is a single variant with c-axis oriented vertical. (B) is a partially twinned crystal showing inactive triangular regions in dark grey. (C) is a partially twinned crystal showing twin-boundaries intersecting upper and lower constraints. In practice, this situation (C) does not arise due to stress concentration in regions highlighted by the red circles.

The most notable difference occurs at the points labeled A and B where the curves become more rounded. Point A and B occur at the inflection points of the plots in Figure 4-4, with Point A being along paths in which the crystal is being compressed (H returning to 0, inflection at high strain) and Point B being the inflection at low strain on the paths corresponding to the crystal extending (H approaching $\pm H_{max}$) in Figure 4-4.

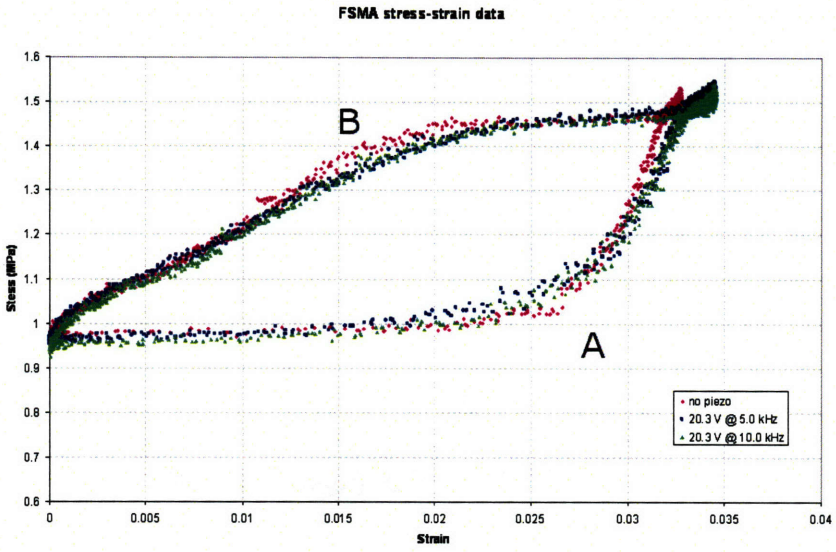

Figure 4-6: Effect of acoustic-assistance on the ϵ vs. σ behavior for a large magnetic field drive on a sample from TL7. This data corresponds with the ϵ vs. H measurements in Figure 4-4

The rounding effect in Figure 4-6 with the additional acoustic energy is believed to arise because defects in the material are able to be overcome at a lower stress with the inclusion of acoustic-assistance. For large defect strengths, a large magnetic or mechanical stress is needed to move a twin-boundary over the defect. The atomic motions caused by the addition of acoustic-assistance allows for obstacles to be overcome at a lower stress value and results in the smoother appearance of the $\sigma - \epsilon$ plots.

The shape of the σ vs. H curves (Figure 4-7) are similar to those in Figure 4-4. At $H = 0$, the stress is equal to the static bias stress of 0.95 MPa. As the field is increased, the stress stays constant until a threshold field is reached. This threshold corresponds closely with the threshold field for strain initiation (Figure 4-4). After the field has reached its maximum value and is decreased, the stress follows the upper curve back to $H = 0$.

The relative insensitivity of the stress-field behavior to the addition of acoustic-assistance is an encouraging result. Chambers found that the acoustically driven strain fell off dramatically at stresses an order of magnitude lower than those used

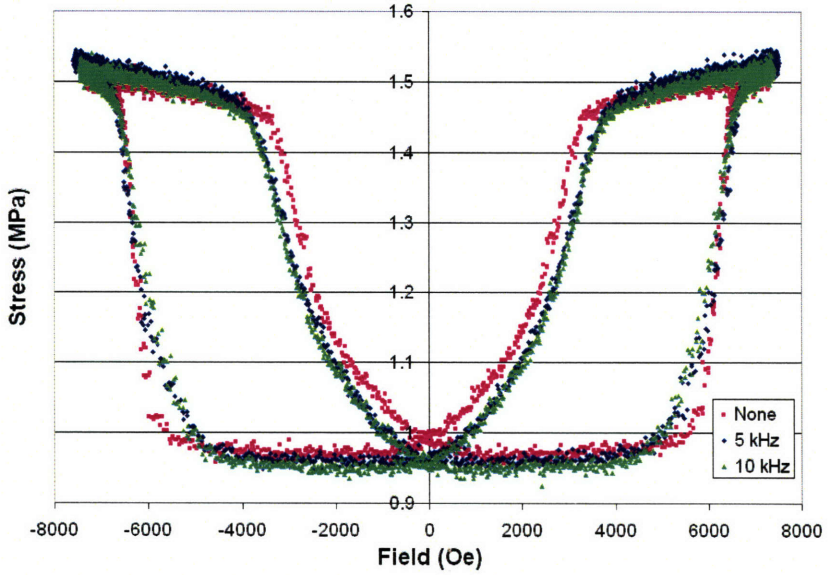

Figure 4-7: Effect of acoustic-assistance on the σ vs. H behavior for a large magnetic field drive on a sample from TL7. The acoustic drive is 20.3 V_{pp} at varying frequencies.

as the bias stress in the above data [15]. Also, these stress shown above are similar to those for pure magnetic drive [25] further indicating no negative effects on the potential FSMA mechanical work output as part of a hybrid device.

4.2.1 Additional Large-Field Results

Similar data as above were taken on a sample of material from TL8 (Figures 4-8 to 4-10). The overall trends were the same. Acoustic-assistance reduced the threshold and increased the strain output. However, the magnitudes of the changes are significantly smaller than for the TL7 sample shown in Figures 4-4 to 4-7.

The threshold field is initially 2750 Oe for the TL8 sample and is reduced to 2520 Oe at the highest frequency acoustic drive (Figure 4-9). There is also no apparent change from 4.6% strain for this sample with the inclusion of acoustic assistance as shown in Figure 4-10.

The wide disparity in acoustic effect between TL7 and TL8 can be correlated closely with the defect concentrations within the samples. Richard has done exten-

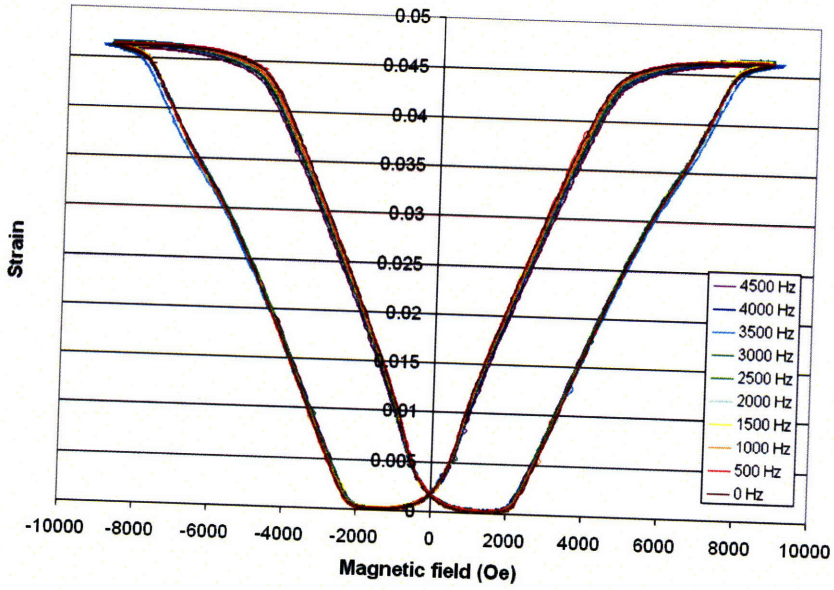

Figure 4-8: Effect of acoustic-assistance on the ϵ vs. H behavior for a large magnetic field drive on a sample from TL8. There is a slight reduction in the threshold as the piezoelectric drive frequency is increased.

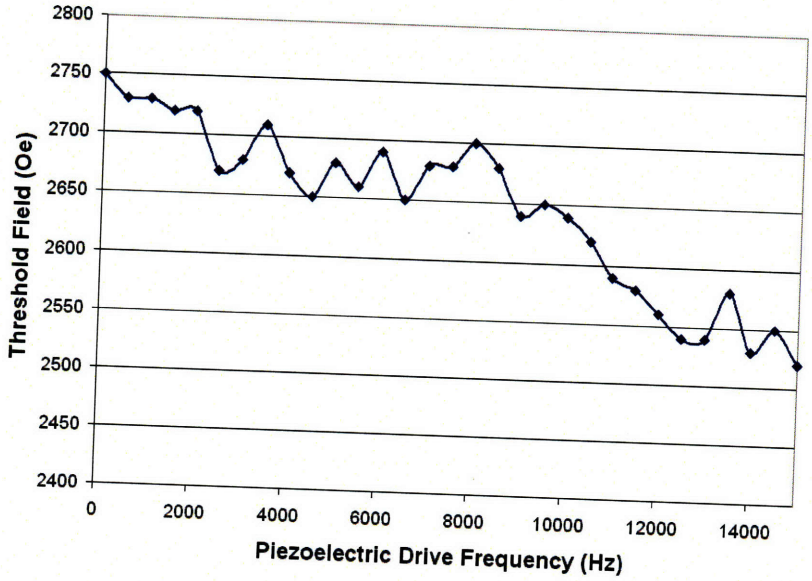

Figure 4-9: Summary of the threshold magnetic field to initiate twin-boundary motion for acoustic-assist frequencies up to 15 kHz, in a sample from TL8. There is a small, 8%, reduction in the threshold as the acoustic-assist frequency is applied up to 15 kHz.

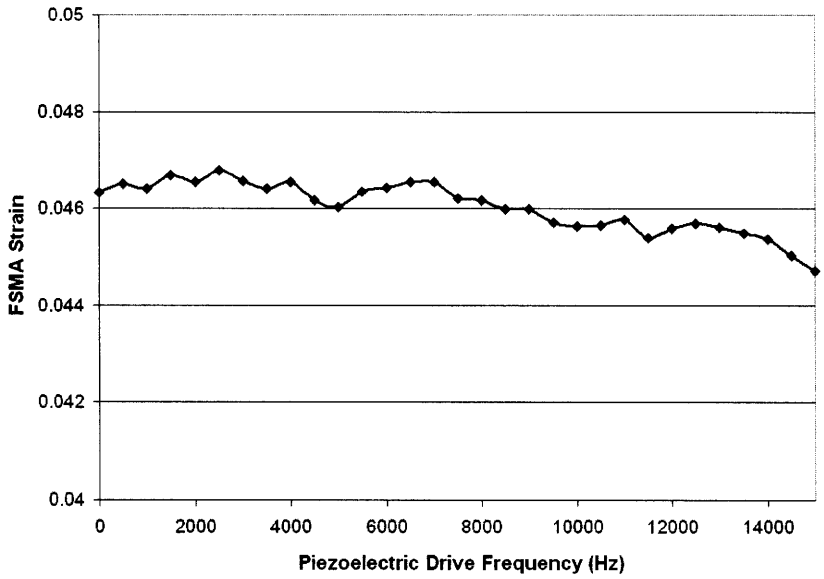

Figure 4-10: Summary of the cyclic strain for acoustic-assist frequencies up to 15 kHz in a sample from TL8. Over a wide range of frequencies, the strain output remains nearly constant at ≈4.6%

sive characterization of the defect concentrations with samples from the same parent crystal boules as those used in these experiments [43]. He showed that each of the crystals contained Ti and S rich precipitates and defects strengths were calculated to be near 0.5 K_u based on simple Orowan models. At this strength, the impurities are not expected to block twin-boundary motion altogether, but may be capable of impeding it. Of the samples tested from these two crystals, TL8 showed the lower concentration of these impurities. TL7 was also shown to have regions of retained austenite [46], which could further impede twin-boundary motion and account for the large threshold fields.

Defects reduce the mobility of twin-boundaries. It is not unexpected that TL8 would therefore have the lower threshold for twin-boundary motion, as it is largely a defect controlled phenomenon. Also, acoustic-assistance primarily affects the potency of these defects in pinning twin-boundaries. It can be assumed then that the magnitude of the acoustic-assistance effect is largely determined by the defect content and that acoustic-assistance has a correspondingly lower effect on the purest and the

lowest threshold of the samples (TL8) as a result. The sample from TL7 contains more numerous second phase defects, and therefore has an initially large threshold and its threshold has a stronger dependence on the acoustic drive than TL8.

A similar effect is found for the output strain. Crystals showing near maximum field-induced strain typically have lower concentrations of defects that can block twin-boundary motion relative to low-strain samples, with all else being equal. Therefore, crystals showing large field-induced strain, of similar composition, should have lower defect concentrations and will see the smallest gains with the addition of acoustic-assistance as acoustic-assistance works by mitigating the effect of defects.

4.2.2 Phase space plots

In the following section, the effects of the piezoelectric drive voltage (which determines the piezoelectric displacement magnitude) and frequency of the acoustic-assistance on FSMA actuation are described. The following data were taken using a 1 Hz magnetic drive, strong enough to saturate Ni–Mn–Ga, and varying acoustic parameters. The FSMA sample from TL7 used has a high initial threshold field of 4600 Oe, and AC-strain of 3.3%.

Figure 4-11 shows the threshold field as a function of the voltage and acoustic frequency parameters. At low acoustic input voltage and frequency, the threshold is initially high at 4600 Oe and reaches a local minimum of 4200 Oe, at 1 kHz and low voltage acoustic drive. The minimum threshold field observed was 3900 Oe in this sample. For all frequencies, the threshold falls off rapidly with increasing piezoelectric drive voltage and little additional reduction is observed for voltages larger than 12 V_{pp} for this sample. Although there is some structure in the frequency dependence, the threshold generally is reduced as the drive power is increased by either an increase in drive voltage or frequency.

The strain as a function of piezoelectric drive voltage and frequency is shown in Figure 4-12. Output strain increases slightly with increased voltage and/or frequency from 3.3% to 3.6% strain. Maximum strain is achieved at the largest voltage and frequency drives, and the magnitude of the change is small over a wide drive voltage

and frequency spectrum, as in previous data with large magnet field drives.

4.3 Energy, Power, and Efficiency Considerations

As was stated earlier (Section 4.1), the addition of acoustic assistance allows for a more efficient conversion of the magnetic energy into useful work. This section uses some simple calculations to determine the extent of this improvement based on the magnetic power input, the mechanical power from the piezoelectric, and the $\sigma - \epsilon$ work output of the FSMA. The magnetic work input is given by

$$W_{mag} = \mu_0 M_s \Delta H \tag{4.2}$$

where M is the magnetization and ΔH is the change in applied field. This equation has a maximum value of

$$W_{mag} = K_u V \tag{4.3}$$

where the magnetic field is increased from zero to the saturation field, where K_u is the magnetic anisotropy and V is the volume of the material. The mechanical work done by the piezoelectric on the FSMA is given by

$$W_p = \epsilon_p \sigma_p V \tag{4.4}$$

where ϵ_p is piezoelectric strain and σ_p is piezoelectric stress. The FSMA work output is given by

$$W_F = \epsilon_F \sigma_F V \tag{4.5}$$

In Eqns 4.2-4.5, and the following equations, the subscript F refers to the value for the FSMA and p for the piezoelectric. For Equations 4.2, 4.3, 4.4, and 4.5, power can be obtained by multiplying each energy by the corresponding angular frequency, ω.

The piezoelectric work can be expressed in terms of more readily known quantities

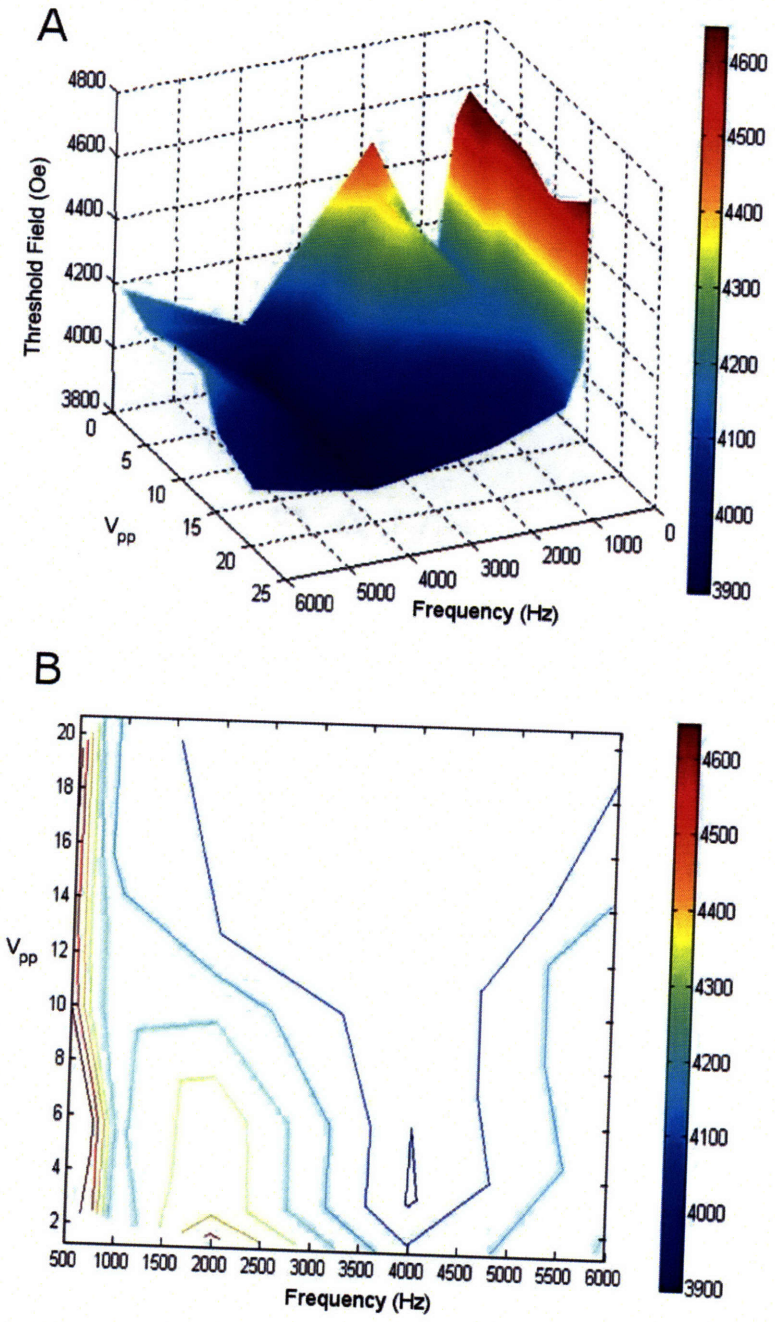

Figure 4-11: Plot showing the dependence of the threshold field on both the applied voltage and frequency to the piezoelectric. Plot B is the contour map of Plot A. The threshold tends to decrease with increases in both voltage and frequency until it reaches an asymptotic value near 3900 Oe. Note that the axis are reversed between Plot A and B.

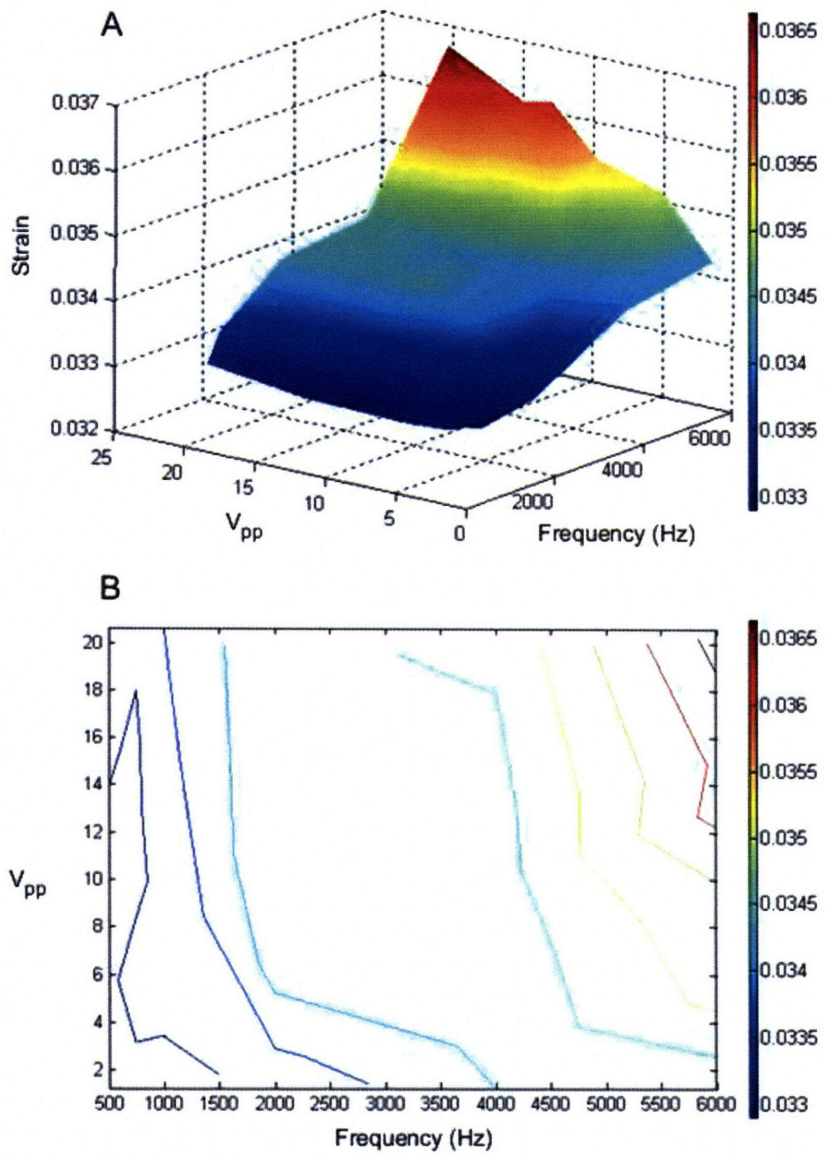

Figure 4-12: Plot showing the dependence of the strain on both the applied voltage and frequency to the piezoelectric. Plot B is contour map of Plot A. Output strain increases with both voltage and frequency, although the magnitude of the change is small.

by recognizing that the position of the end of the piezoelectric, x, is given by

$$x = (\Delta L)\sin(2\pi ft) \tag{4.6}$$

$$v = \frac{dx}{dt} = 2\pi f(\Delta L)\cos(2\pi ft) \tag{4.7}$$

from which we can derive the velocity and acceleration:

$$a = \frac{dv}{dt} = -(2\pi f)^2(\Delta L)\sin(2\pi ft) \tag{4.8}$$

Here ΔL is the amplitude of the piezoelectric stack displacement and in general is a function of the applied voltage and frequency. The average acceleration at the end of the piezoelectric can then be estimated in terms of its RMS value as

$$a_{rms} = 0.707(2\pi f)^2(\Delta L) \tag{4.9}$$

Incorporating this acceleration into the stress in Eqn. 4.4 yields

$$W_p = \frac{F}{A}\epsilon_p V = \frac{M_F\, a_{rms}}{A}\epsilon_p V \tag{4.10}$$

$$W_p = \frac{0.707 M_F(2\pi f)^2(\Delta L)\epsilon_p V_p}{A_F} \tag{4.11}$$

Here M_F is the mass of the FSMA that is put in motion by the action of the piezoelectric. The mass of the other moving parts can also be included in M_F. Eqn. 4.11 can then be reduced to

$$W_p = \frac{0.707 M_F(2\pi f\epsilon_p)^2 V_p L_p}{A_F} \tag{4.12}$$

and as before, the power transferred from the piezoelectric to the FSMA can be determined

$$P_p = W_p\omega = \frac{0.707 M_F(2\pi f)^3\epsilon_p^2 V_p L_p}{A_F} \tag{4.13}$$

Table 4.1 shows the analysis of power inputs and outputs for the data presented earlier in Figure 4-4, Figure 4-6, and Figure 4-7. It can be seen that the addition of

acoustic-assistance improves the efficiency of the FSMA by only a small amount when calculated for a full $\epsilon(H)$ loop. With the addition of a 5 kHz and 20 V_{rms} acoustic drive, the FSMA power output increases by an amount about equal to the acoustic drive power and overall efficiency is improved 0.5% (absolute change in efficiency). Increasing the acoustic frequency, f, from 5 kHz to 10 kHz, the FSMA efficiency falls off due to the large increase in power from the piezoelectric with no change in FSMA output, indicating that the piezoelectric's effect on efficiency depends strongly on the operating conditions of the piezoelectric. This is especially true of the piezoelectric drive frequency because the mechanical power supplied from the piezoelectric scales as the frequency cubed and the square of the voltage (Eqn. 4.13), as $V \propto \epsilon_{piezo}$.

Power calculations for a small-amplitude acoustic drive, 2.7 V_{rms}, are presented in Table 4.2. For the operating conditions, the FSMA strain ranged from 3.3% for the 50 Hz acoustic drive to 3.45% strain for the larger acoustic drives and the $\Delta\sigma$ was approximately 0.33 MPa for all cases. The low piezoelectric drive voltage is responsible for the low piezoelectric mechanical power even at 10 kHz. The mechanical power from the piezoelectric accounts for only 3% of the total power input at the highest drive frequencies. The difference in FSMA efficiencies between the data at 50 Hz and 5 kHz is +0.33%, and the efficiency is essentially constant for all higher frequencies. It is interesting to note that an improvement in FSMA output power of 0.9 mW is achieved with an addition of as little as 0.076 mW of mechanical power from the piezoelectric.

The change in overall efficiency is mainly a result of the strain increase with the addition of the piezoelectric drive. Therefore, the largest change in efficiency would be found when the strain changes by a large fraction, as in Figure 4-1. No stress data was acquired for the data set presented in Figure 4-1, but by assuming the same $\Delta\sigma$ of 0.33 MPa, estimates of the efficiency can be made. In Table 4.3, the addition of the piezoelectric drive causes a near doubling of the efficiency from 5 V drive to the 55 V drive.

Additional energy savings can be achieved by a reduction in power requirements needed to generate a specified FSMA strain value as the inclusion of a piezoelectric

drive reduces the magnetic field amplitude required. Eqn. 1.10 shows that the minimum power required to operate a given magnet scales as the square of the magnetic field. Reducing the threshold/operating field can therefore result in large power savings. A reduction in required field of as little as 5% corresponds to a ≈10% power savings.

For the FSMA actuators, the ratio of overall input energy to mechanical output compares well with that of conventional piezoelectric actuator devices. Wang reports a 6.1% theoretical efficiency of electrical energy to output mechanical energy conversion for a cantilever bimorph made from soft PZT ceramic (Motorola 3203HD) and measured values of 6.0% [47]. Adhesively-bonded PZT and PMN (lead magnesium niobate) stacks have been found to have efficiencies of 17–27% [48].

Piezo/Acoustic Frequency	Magnetic Power	Piezo Power	Power Output	Efficiency
none	283 mW	0 μW	27.8 mW	9.84%
5000 Hz	283 mW	0.49 μW	29.3 mW	10.38%
10000 Hz	283 mW	3.95 μW	29.3 mW	10.38%

Table 4.1: Power calculations based on the data presented in Figure 4-4 with a 20.3 V_{rms} piezoelectric drive.

Piezo/Acoustic Frequency	Magnetic Power	Piezo Power	Power Output	Efficiency
50 Hz	283 mW	≈0 mW	20.8 mW	7.34%
5000 Hz	283 mW	0.02 μW	21.7 mW	7.67%
7500 Hz	283 mW	0.08 μW	21.7 mW	7.67%
10000 Hz	283 mW	0.20 μW	21.7 mW	7.67%

Table 4.2: Power calculations based on the data driven to magnetic saturation with a 1 Hz drive frequency and with a 2.7 V_{rms} piezoelectric drive at varying frequencies.

Piezo Voltage	Magnetic Power	Piezo Power	Power Output	Efficiency
5 V_{pp}	170 mW	≈0 μW	14.6 mW	8.57%
35 V_{pp}	170 mW	0.007 μW	19.6 mW	11.48%
55 V_{pp}	170 mW	0.015 μW	24.9 mW	14.58%

Table 4.3: Power estimates based on $\Delta\sigma$ = 0.33 MPa for the data presented in Figure 4-1. The piezoelectric was driven at 1 kHz.

Chapter 5

Finite-Element Simulations

In order to adequately characterize the actuation behavior of Ni–Mn–Ga crystals as a function of frequency, it is important to know the resonant behavior of the test fixture. Resonant modes are unavoidable to a large degree and must be known in order to separate the intrinsic material behavior from that of the test device. This chapter describes 3-D finite element modeling (FEM) of the dynamic behavior of the $X4$ actuator at various frequencies. The lowest frequency resonant modes were determined to be due to the off-axis displacements of the compression spring in the system.

5.1 Quasi-static deformation

The finite-element modeling (FEM) of the stress distribution was used to analyze the deformation of the bodies within the load path. The FEM results also serve as a validation that the model is behaving appropriately for the frequency analysis described later in this chapter.

In order to carry out these simulations, a 3-D model of moving parts in the apparatus was constructed in ProE® and imported into ANSYS® Workbench, where the finite-element simulations were carried out. Typical material properties for the components were assigned to the geometry from within ANSYS® and all of the materials were assumed to be linear elastic and isotropic; the untwinned FSMA stiffness was

Number	Material	Density (kg/m^3)	Stiffness (GPa)	Poisson's Ratio
1	Steel	7850	200	0.3
2	Fiberglass	1500	100	0.3
3	Aluminum	2700	70	0.3
4	FSMA Crystal	8400	65	0.3
5	Piezoelectric Stack	7000	60	0.3

Table 5.1: Material properties used in ANSYS® Workbench simulations.

used, see Table 5.1. Figure 5-1 shows how these material properties were assigned to elements in the $X4$ actuator.

Physical constraints were then applied to the model. The top of the spring, the bottom of the piezoelectric, and the right ends of both of the flexures (where the mobile parts in the load path are connected to the rigid frame of the apparatus) were all constrained to be immobile in the three orthogonal directions. The loading to the system from the FSMA actuation was then applied as a 0.4 mm displacement on the top surface of the FSMA which corresponds to a 3.3% FSMA strain. These initial conditions are shown in Figure 5-2 and the mesh used is shown in Figure 5-3. Initial conditions can impact the results of the simulation considerably and were chosen to most closely match the physical system.

At each interface between volumes/components, the contacting areas were defined as bonded to prevent slippage on those planes. The only exception was the spring-upper flexure interface which was defined as "rough" to allow for the two components to come out of contact and to undergo limited sliding when they are in contact.

The FEM model was then evaluated to determine the quasistatic strains in the apparatus. Figure 5-4 shows the calculated deformation in the vertical, x-direction, of the apparatus under the above conditions. Note that the extension of the FSMA causes primarily rigid body motion of the steel components above it. Deformation is primarily confined to vertical displacement of the spring flexures on the right side of the device and the compression of the spring in the load path. This is the way the apparatus was designed to operate. The flexure extending to the left stays level and is undeformed, which confirms that the flexure used to measure strain does not amplify the strain from the crystal under quasi-static conditions. It moves up in conjunction

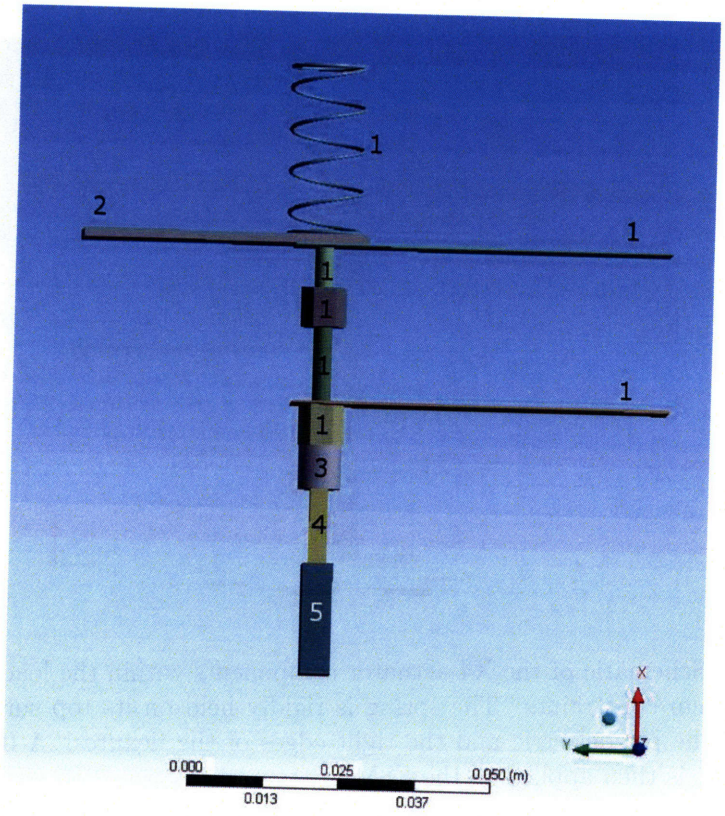

Figure 5-1: Schematic of the material distribution in the X4 actuator. Material properties are summarized in Table 5.1

with the FSMA extension giving an accurate displacement measurement.

5.2 Frequency Analysis

In order to fully characterize the response of the system at various frequencies, the resonant modes must be determined. These modes have a strong impact on the shape of the $\epsilon - H$ and $\epsilon - f$ behavior of the system and need to be understood in order to interpret the data accurately. To do the analysis, ANSYS® Workbench "Frequency Finder" solution method was applied to the same model used for the quasi-static analysis. The first four resonant modes of the system were determined.

The lowest frequency mode is shown in Figure 5-5. It is a spring bending mode at 73.7 Hz whose motion is at 45° to the plane of the page. In this mode, the top surface

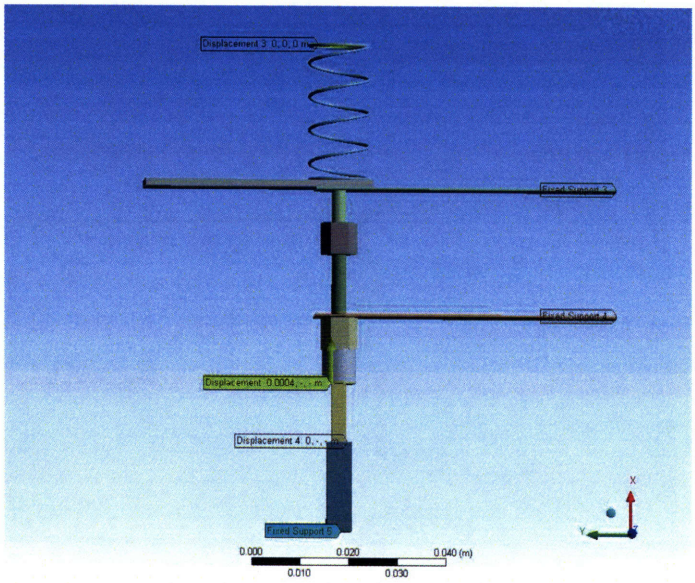

Figure 5-2: Schematic of the X4 actuator components within the load path with the applied system constraints. The spring is rigidly held on its top surface as are the surfaces of the piezoelectric and the right edges of the flexures. A 0.4 mm vertical displacement is then applied to the FSMA.

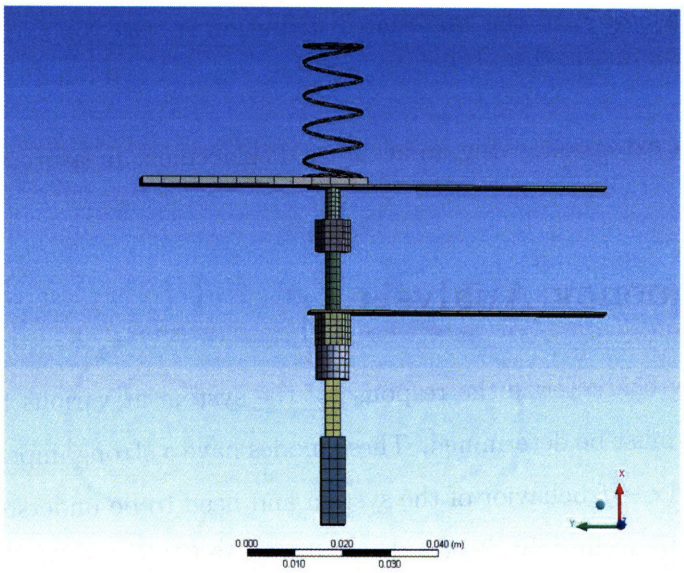

Figure 5-3: Schematic of the mesh applied to the X4 actuator geometry as it was used in the ANSYS® Workbench analysis.

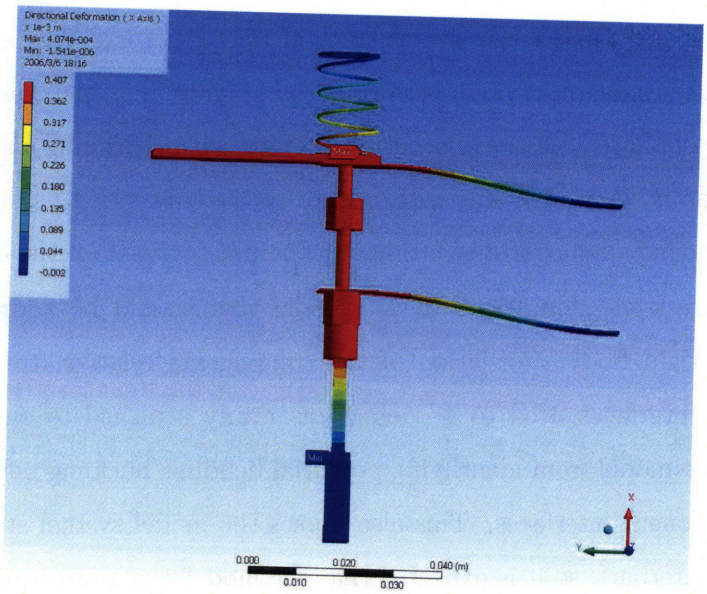

Figure 5-4: U_x displacement (displacement in the vertical direction) caused by the extension of the FSMA crystal.

of the spring is fixed, and the lower section of the spring vibrates in bending. The extent of the deformation in Figure 5-5 is exaggerated by ANSYS® for illustrative purposes and the true deformation magnitude is small. Also, only the motion of the resonant parts are shown. Mode 2, at 73.8 Hz, is similar to that in Figure 5-6 but the spring bending motion occurs in the plane perpendicular to the mode 1 deformation.

Figure 5-7 shows the third resonant mode at 193.6 Hz. This is the longitudinal compression-extension mode arising from inertial forces acting on the spring. It is especially problematic for the device operation as it results in a loss of spring load on the Ni–Mn–Ga crystal and therefore an inability to reset the sample. The next mode is an expansion mode of the spring at 206.1 Hz (Figure 5-8).

The first mode not associated with the compression spring, and the 21st overall, occurs at 864 Hz and is the first buckling mode ($n = 0$) deformation in the upper spring flexure, Figure 5-9.

It is important to note that the first 20 of the identified resonant modes and all of the modes within the operation range of the device are associated with the coil spring in the system and not the FSMA material or other parts of the system. It is these

modes which will impact the performance of the actuator device most significantly and will lead to a degradation in performance at higher frequencies as the components become out of phase with one another. Therefore, when designing an actuator, special consideration needs to be made with respect to the bias spring used as it will dictate the low-frequency behavior and ultimately the upper bound of the operating range.

There are some limitations to the model that should be addressed. In order to prevent rigid body translation of the components relative to one another, the component interfaces need to be defined as firmly attached to one another. This precludes the model from identifying potential bending/buckling behavior, especially at the component interfaces. This also makes the model system stiffer overall than the real counterpart, so it is expected that the model may overestimate the resonant frequencies or miss low frequency bending/buckling modes. The model, for simplicity, also does not account for the rigid exterior frame structure. As a result, primarily low-frequency modes of the frame, to which the modeled parts are affixed, will be missed.

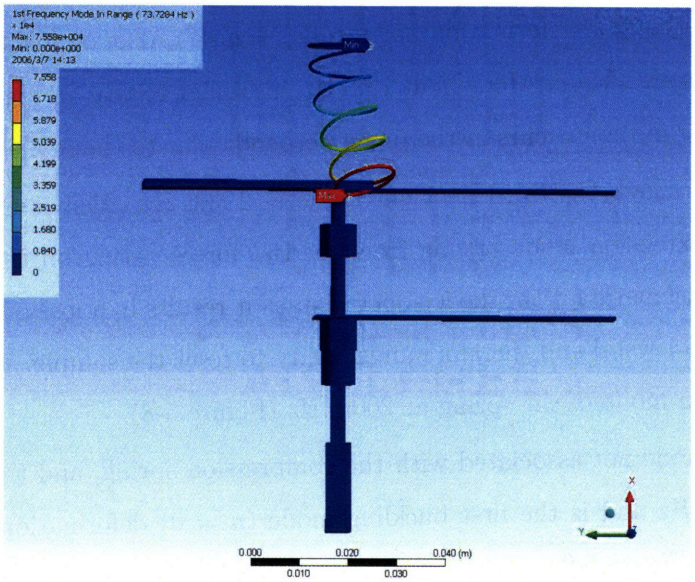

Figure 5-5: First resonant mode of the system at 73.7 Hz which is a spring bending mode at 45° to the plane of the page. The extent of the deformation is exaggerated by ANSYS® for illustrative purposes.

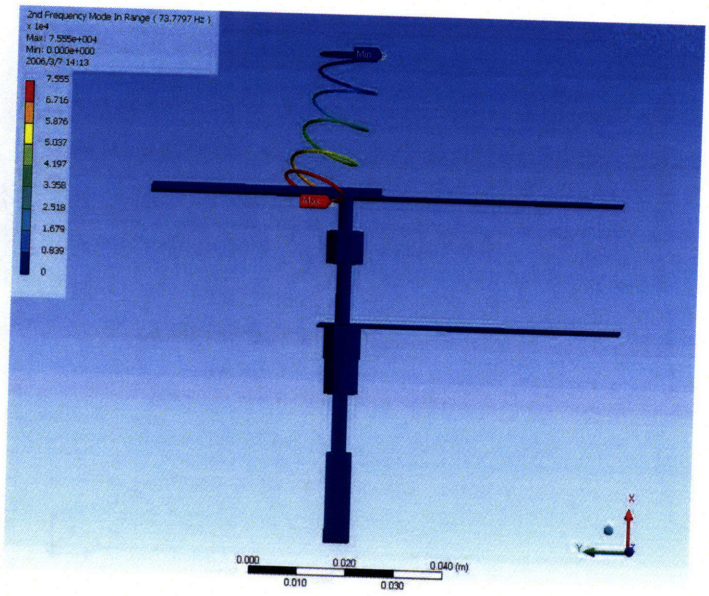

Figure 5-6: Second resonant mode of the system at 73.8 Hz which is a spring bending mode perpendicular to the first mode. The extent of the deformation is exaggerated by ANSYS® for illustrative purposes.

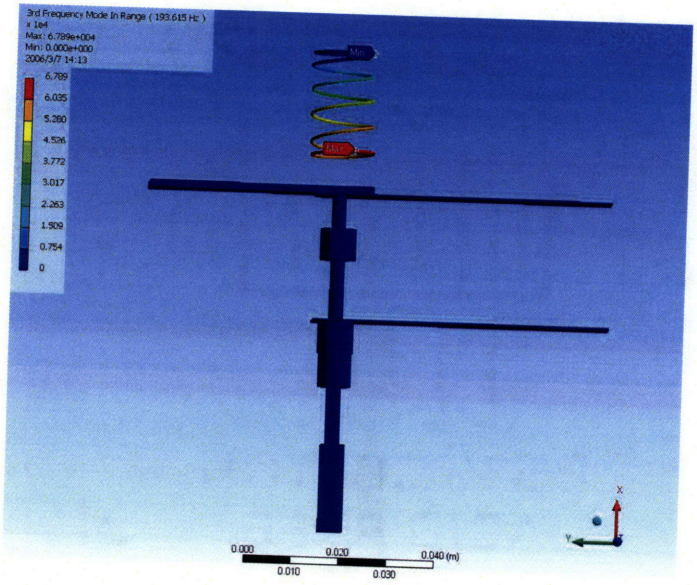

Figure 5-7: Third resonant mode of the system at 193.6 Hz which is a longitudinal compression-extension spring mode. The extent of the deformation is exaggerated by ANSYS® for illustrative purposes.

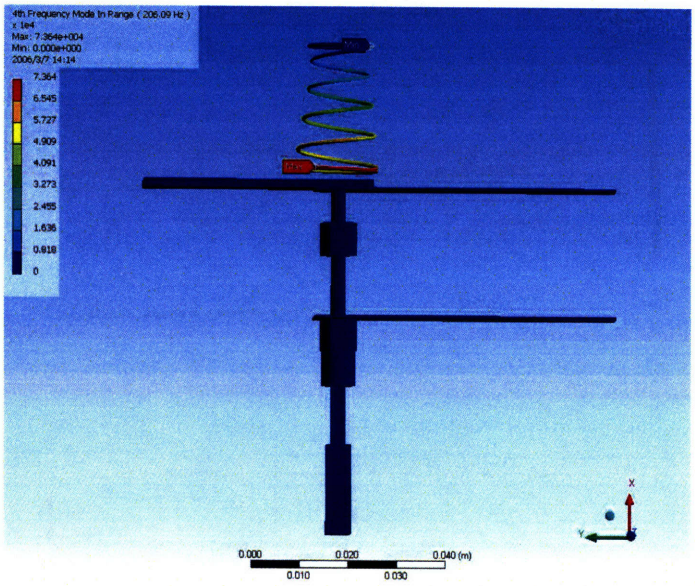

Figure 5-8: Fourth resonant mode of the system at 206.1 Hz which is a bowing/expansion spring mode. The extent of the deformation is exaggerated by ANSYS® for illustrative purposes.

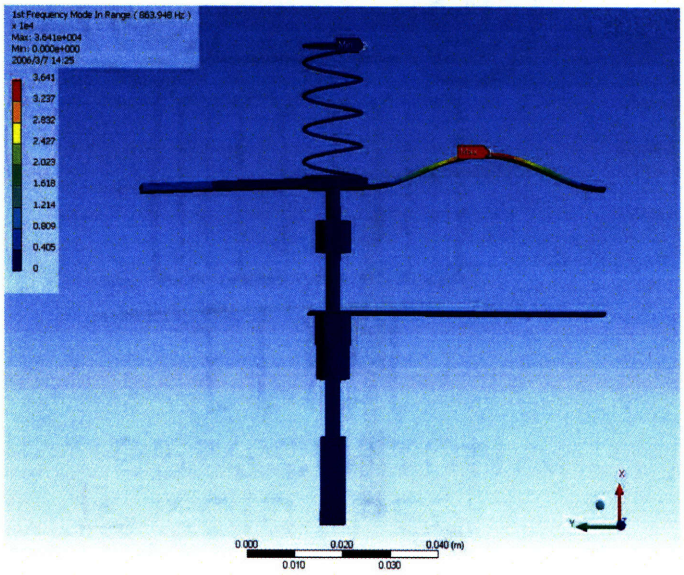

Figure 5-9: First non-compression spring resonant mode of the system at 864 Hz which is a buckling mode of the upper flexure. The extent of the deformation is exaggerated by ANSYS® for illustrative purposes.

In order to increase the resonant frequencies of the spring, a stiffer spring can be used in its place. This will drive up the resonant frequencies of the spring and give a larger bandwidth to the actuator. However, there is a trade-off. With a stiffer coil spring, a smaller displacement is required for the spring stress to approach the blocking stress in Ni–Mn–Ga for twin boundary motion. Therefore, there is a trade-off between actuator stroke and bandwidth with the use of a coiled compression spring. A large bandwidth in an actuator of this design requires that the stroke be small, while an actuator optimized for large stroke will inherently have a smaller maximum operating frequency.

However, much of this tradeoff can be eliminated by small changes in the actuator design. Optimally, a coiled compression spring should be avoided altogether in the system if one wants good high-frequency performance, due to the low intrinsic resonant frequencies of coil springs. A better design method employs the use of a leaf spring or Belleville spring to supply the reset force. These springs have the advantage of large stiffness perpendicular to the primary deformation direction, unlike coil springs, and typically have a significantly larger initial resonant frequency.

Based on the ANSYS® model results, the system was redesigned to substitute a leaf spring for the coil spring. This design also allows for the removal of the capitance gauge extension (shown extending to the left in Figure 5-1) as the capacitance gauge can now be placed in the load path where the coil spring was previously located. The new actuator geometry that incorporates the leaf spring is shown in Figure 5-10.

The width of the leaf spring was optimized independently in ANSYS®, such that a 6.75×62 mm free length of a steel spring supplies 3 MPa of stress on the crystal when the crystal extends 0.4 mm. Using a number of simulation runs, the resonant frequency was found to fit the linear equation

$$f_{res} = 211.63t + 5.3025 \tag{5.1}$$

where t is the thickness of the leaf spring in millimeters and f_{res} is in Hz. The displacement of the end of the spring (mm) under a 13 N load (which corresponds to

approximately to a 3.0 MPa stress on the crystal) was found to vary as

$$\Delta x = 8.979t^{-2.9892} \tag{5.2}$$

Setting the desired displacement to 0.4 mm, these indicated that the appropriate width of the spring was 2.8 mm and that the first resonant mode occurs at 598 Hz.

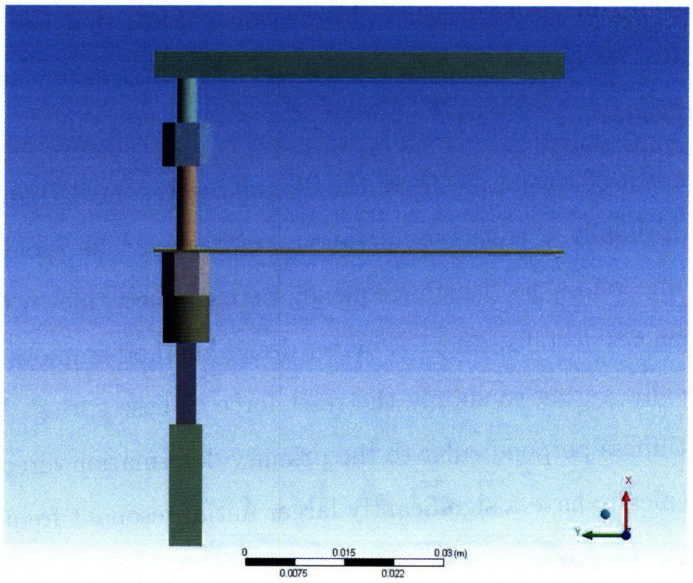

Figure 5-10: Geometry of the modified $X4$ actuator with a leaf spring as the upper most flexure in the schematic. The coil spring and cap gauge extension have been removed compared to the previous design.

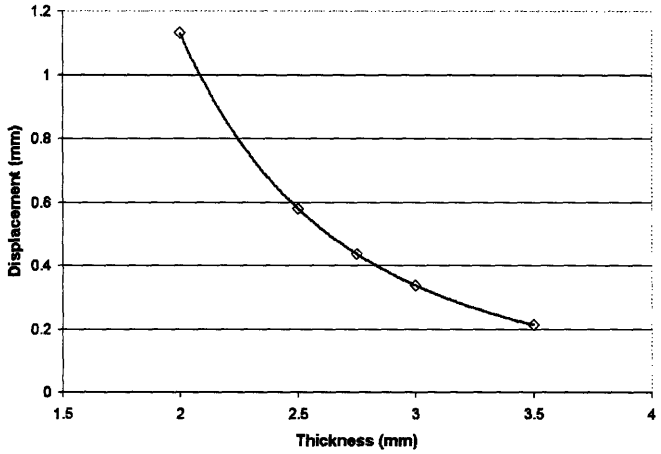

Figure 5-11: Displacement of the end of the leaf spring under a 13 N applied bending load. The trend line shown corresponds to Eqn. 5.2.

Chapter 6

High-Frequency Actuation

Previously discussed data indicate that there are significant gains that can be obtained by the addition of a high-frequency piezoelectric drive to Ni–Mn–Ga driven magnetically at 1 Hz. This is particularly true if the FSMA sample has a relatively high threshold field for actuation. In the following chapter, the effect of the piezoelectric is described at actuation frequencies from 1–500 Hz on the $X4$ apparatus modified with the inclusion of a leaf spring.

6.1 High-Frequency Data at Saturating Magnetic Fields

Using the $X4$ apparatus described in Chapter 3.2.2, data were collected using a $2.5 \times 4 \times 16.3$ mm crystal from TL8. The magnetic field was applied parallel to the 4 mm dimension within the experimental apparatus. Figure 6-1 shows a single loop from each of the separate test runs taken at various actuation frequencies in the range 1–200 Hz; the cyclic strain is summarized in Figure 6-3.

The 1–50 Hz loops have the same general shape as those previously measured at 1 Hz on the $X1$ apparatus (see Figure 4-8) and show a strain of roughly 0.0175 (1.75% strain) over that range. The threshold field (1500 Oe) is lower than previously measured, due mainly to relative ease of magnetizing this sample compared to the

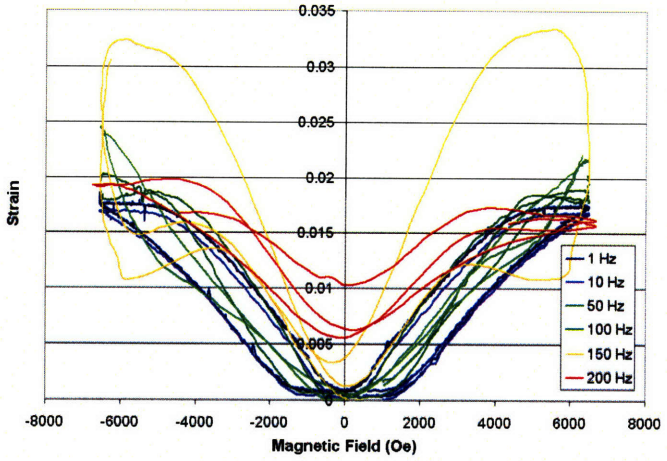

Figure 6-1: Strain as a function of applied field on the $X4$ actuator for various magnetic drive frequencies. Peak magnetic field value is 6.5 kOe and there was no piezoelectric drive used in this data set.

previous ones. The easier magnetization of the sample is a result of its cross-sectional shape which generates a weaker demagnetization field. Previous samples had a square cross section while this sample has a rectangular cross section with the long direction oriented parallel to the magnetic field.

The FSMA shows considerably larger strain at 150 Hz than at the other frequencies. As can be seen from Figure 6-1, the shape of the curve also changes dramatically, suggesting the presence of a system resonance. Even after the field reaches its maximum value, the strain continues to increase, suggesting inertia in the FSMA and spring. This is followed at 200 Hz by the corresponding anti-resonance and a large reduction in output strain relative to the other frequencies. Comparing the 150 Hz resonant frequency to the model in Chapter 5.2, this frequency does not correspond to any of the resonant modes identified in the ANSYS® simulations. It is therefore possibly a bending mode of the system at a component interface, as the model did not take into account these bending modes due to difficulty with modeling the interfaces properly. Bending modes are also expected to occur at relatively low frequencies because of the weak lateral constraints on the components in the load path.

Figure 6-2 shows the change in strain output with the addition of acoustic-

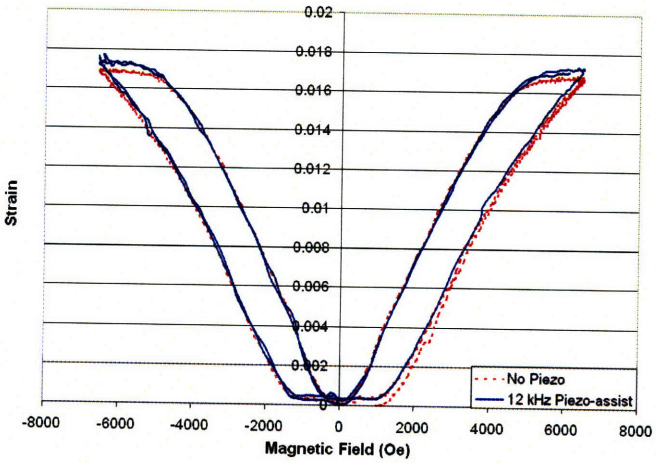

Figure 6-2: The effect of a 12 kHz acoustic-assistance at 15 V_{rms} for a 10 Hz actuation frequency. The maximum applied field is 6.5 kOe.

assistance for the crystal driven magnetically at 5 Hz. The piezoelectric is driven at 12 kHz at an amplitude of 15 V_{rms}. The addition of this piezoelectric drive yields a 4.4% increase in relative strain output. The decrease in threshold field is larger than the increase in strain, though not as large as the approximately 1 kOe decrease in crystals that start with a higher initial threshold field.

Overall though, the addition of the piezoelectric drive has little effect on the output strain as seen in Figure 6-3. This is not unexpected as 8 kOe magnetic fields (sufficient for saturation) are being applied to the crystal. As with the previous low-frequency data (Figure 4-4 and Figure 4-8), when magnetic fields that are capable of causing saturation are used, the crystal shows little improvement in output strain when acoustic energy is applied. The crystal has already strained to a large fraction of its total possible strain under the given applied load prior to the application of the acoustic drive.

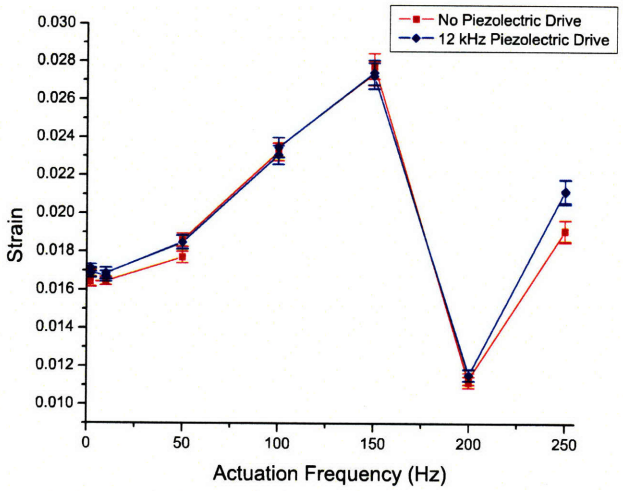

Figure 6-3: Summary of the cyclic strain from the data presented in Figure 6-1 along with the effect of piezoelectric drive included. Peak magnetic field value is 6.5 kOe. Diamonds are with acoustic assistance and squares are the control experiments without acoustic assistance. Error bars represent one standard deviation.

6.2 High-Frequency Data at Non-Saturating Magnetic Fields

The acoustic effect was also measured at fields below those needed to saturate Ni–Mn–Ga. For this set of experiments, a maximum magnetic field of 3.1 kOe was used which produced one-third the output strain as the experiment described above at 1 Hz. Results are shown in Figure 6-4.

As seen before (Figure 6-3), there is a system resonance near the 150 Hz actuation frequency (Figure 6-4). The cyclic strain also increases as the actuation frequency is increased from 400 to 500 Hz. By examining the Fourier transform of the strain waveforms, a large component at 580 Hz is found in addition to the one at the principle frequency within this range of data. The Fourier transform of the strain data is shown in Figure 6-5, with a strong mode at 580 Hz. The 580 Hz signal also tends to persist and ring-down after the magnetic field drive ceases. Looking at the ANSYS® models (Eqn. 5.1), this frequency corresponds closely with the expected value of the leaf

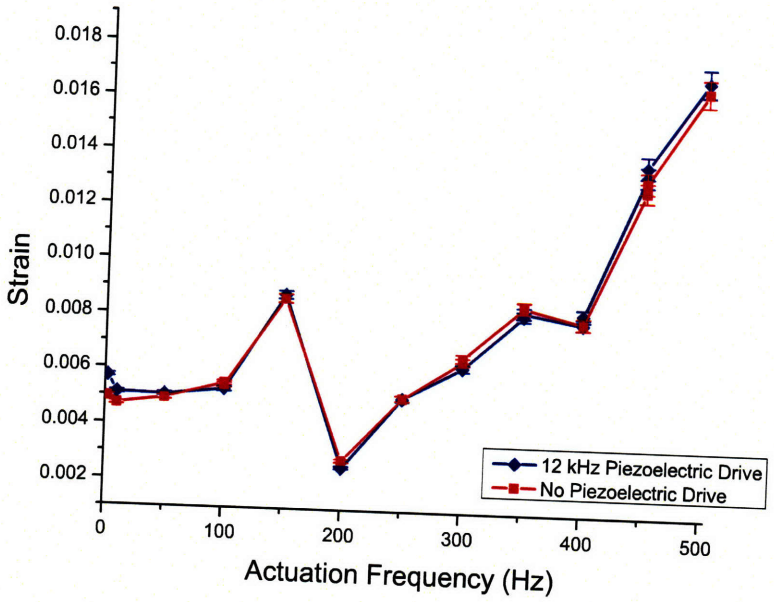

Figure 6-4: Summary of the cyclic strain at 3.1 kOe drive field for actuation frequencies up to 500 Hz. Diamonds are with acoustic assistance and squares are the control experiments without acoustic assistance. Error bars of one standard deviation are used.

spring resonance at 598 Hz. In addition, because the strain measurement is taken from a target affixed to the leaf spring, its resonances will readily be measured within the data. Therefore, the increase in measured FSMA strain, approaching 500 Hz, may be attributed to the excitation and ringing of the leaf spring, rather than a true increase in FSMA strain output. The FSMA strain therefore would be largely constant at 0.006–0.008 over this range if the leaf spring were not resonating.

Comparing the increase in strain amplitude between the case with acoustic-assistance and the control data without, there is a small increase in strain from the additional piezoelectric drive. Previously on the $X1$ data taken at 1 Hz, it was shown that the piezoelectric is most effective for low-magnitude magnetic field drives (Chapter 4.1 and 4.2). The same result is observed on this data taken with the $X4$ actuator, Figure 6-3 and 6-4.

At 1 Hz and 5 Hz, the piezoelectric drive causes a relative increase in strain of

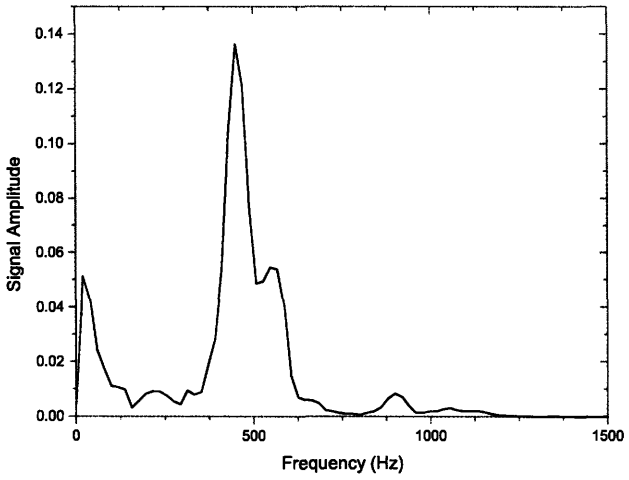

Figure 6-5: The Fourier transform of the strain vs. time data at 450 Hz actuation. The leaf spring resonance is observed near 580 Hz, in addition to the peak for the principle actuation frequency at 450 Hz.

5% and 5.5%, respectively, for a ±3.1 kOe magnetic field drive. This is roughly twice the improvement in relative strain output compared to the data shown above with (±6 kOe) magnetic field drive. As was found in the low-frequency data, small changes in the twin-boundary threshold have the largest impact on the output strain when magnetic field magnitudes near the threshold are used. Also, this effect is most significant when the threshold field is large.

For both values of the maximum magnetic field drive tested (3.1 and 6.5 kOe) on the $X4$ apparatus, the piezoelectric drive is most effective for the lower drive frequencies. The greatest gains in strain are observed at 1 Hz and 5 Hz with essentially zero gain for larger actuation frequencies, specifically $10 < f \leq 500$ Hz. For drive frequencies greater than 50 Hz, the change in strain with the addition of the piezoelectric drive is negligible and within the error of the experiment.

It is believed that the falloff in strain improvement at larger frequencies is the result of two main factors. The first is that the strain measured at higher frequencies is that of the device output and not specifically of the FSMA itself. As a result, the measured strain is affected by system behavior as well as the behavior of Ni–Mn–Ga.

This is most noticeable at 150 Hz where the system goes through a resonance.[1] For frequencies greater than 100 Hz, much of the measured behavior is a result of the overall dynamic system behavior rather than a material property of the FSMA.

The second reason for the falloff in strain improvement with increasing magnetic drive frequency is that there are fewer acoustic cycles per magnetic actuation cycle as the magnetic drive frequency is increased. For a 1 Hz magnetic drive, there are 6000 acoustic cycles per actuation loop. As the magnetic actuation frequency reaches 500 Hz, this number drops to 24 acoustic cycles per actuation loop. Therefore, the internal displacements caused by the acoustic drive have fewer opportunities to assist the magnetic drive in overcoming any defects (by two orders of magnitude) in the material during each actuation cycle. Twin-boundary motion is a stochastic process and the reduction in number of piezoelectrically driven internal displacements reduces their opportunities to effect twin-boundary mobility. Equivalently, the total acoustic energy input (piezoelectric power divided by number of piezoelectric cycles) per magnetic actuation cycle is smaller.

This general roll-off in performance of the acoustic drive with increasing magnetic frequency would seem to indicate that the ratio of the magnetic drive frequency to the acoustic drive frequency is an important quantity. Unfortunately, this is impossible to test with the current experimental apparatuses. In order to keep the ratio constant for a magnetic actuation frequency as small as 20 Hz, a 120 kHz piezoelectric drive would be required, which is above the operating range of the piezoelectric stacks.

For both the ± 6.5 and ± 3.1 kOe magnetic drive amplitudes, the FSMA actuator shows large strains out to the 500 Hz actuation frequencies. The FSMA is able to actuate with the magnetic field out to the 500 Hz actuation frequency and the features in the strain response appear to be solely the result of system resonances. The data at 1–10 Hz on the $X4$ apparatus (Figure 6-3) agree well with the data presented previously in Chapter 4.2 which was taken at similar actuation frequencies. The piezoelectric is most effective in increasing strain output when combined with a magnetic field amplitude that is substantially below the saturation field.

[1]The first FSMA resonance is not expected to occur until $f = \frac{1}{2\pi L}\sqrt{\frac{E}{\rho}} = 27.2$ kHz.

6.2.1 Twin-boundary Velocity

Marioni [11] observed the maximum extensional velocity of the free end of a Ni–Mn–Ga single crystal, in the absence of an external load, to be roughly 6 m/s based on both theory and experimental findings. The velocity of the moving parts of the $X4$ apparatus under magnetic actuation can be easily determined and used as a method of determining the extent to which the actuator is limiting the frequency response of the FSMA.

The position of the end of the crystal and the velocity of the sample from the previous ± 3.1 kOe data taken at a 500 Hz actuation is plotted in Figure 6-6. Figure 6-6 shows a peak extensional velocity of roughly 0.4 to 0.5 m/s at 500 Hz actuation in the absence of an acoustic drive.

The peak velocity as a function of actuation frequency is plotted in Figure 6-7 for the strain data presented in Figure 6-4. A linear increase in velocity with frequency is expected for a sample with constant strain output. As can be seen in Figure 6-7, the velocity deviates from linearity at a number of frequencies (namely 150 Hz and above 400 Hz) which correlate with the resonant frequencies identified above in the strain response, as would be expected. The maximum velocity of 0.58 m/s occurs at 500 Hz, which is well below the theoretical maximum of 6 m/s determined by Marioni [11].

However, Marioni's theoretical analysis was done on a free sample, in which case the kinetic energy is equivalent to the maximum magnetic energy that can be applied to Ni–Mn–Ga. This approach does not account for the effect of an external load on the sample or additional moving mass other than the FSMA. The analysis presented by Marioni can be extended to account for the external load by assuming that the input magnetic energy is equivalent to the sum of the kinetic energy and FSMA strain energy such that

$$E_{mag} = E_{kinetic} + E_{strain} \tag{6.1}$$

$$K_u V = \frac{m_T v^2}{2} + \sigma \epsilon V \tag{6.2}$$

$$K_u V = \frac{m_T v^2}{2} + S\sigma^2 V \tag{6.3}$$

$$|v| = \sqrt{\frac{2(K_u V - S\sigma^2 V)}{m_T}} \tag{6.4}$$

where $S = 1.5 \times 10^{-8}$ Pa^{-1} is the FSMA compliance during twin-boundary motion[2], V is the FSMA volume, m_T is the FSMA mass plus the mass of the other moving parts in the system, σ is the applied stress, v is the velocity, and $K_u = 1.5 \times 10^5$ J/m^3 is the magneto-crystalline anisotropy. Using values appropriate for the $X4$ design, Eqn. 6.4 indicates that the peak theoretical velocity should be approximately 2 m/s.

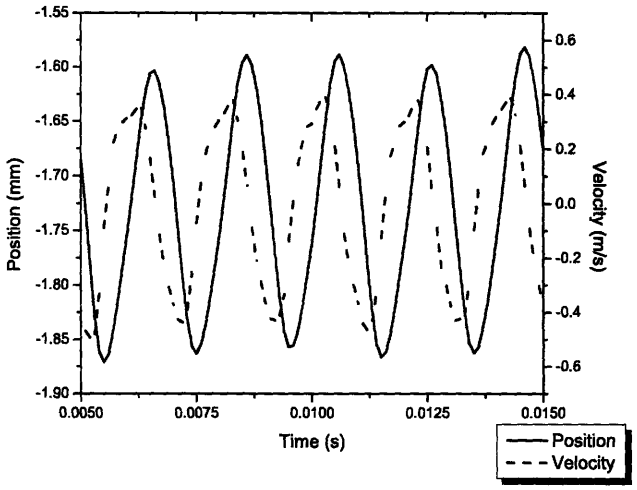

Figure 6-6: Velocity and position of the end of the FSMA crystal under the application of a 250 Hz, ±3.1 kOe magnetic field drive.

6.2.2 Dependence of FSMA extensional velocity on the moving mass and stress

A sensitivity analysis can be performed using Eqn. 6.4 to determine the maximum FSMA velocity as a function of both the applied stress and ratio of the total moving mass in the system to the FSMA mass ($\frac{m_T}{m_{FSMA}}$). As expected, Figure 6-8 shows that

[2]which would correspond to a stiff crystal with a twinning stiffness of C =70 MPa

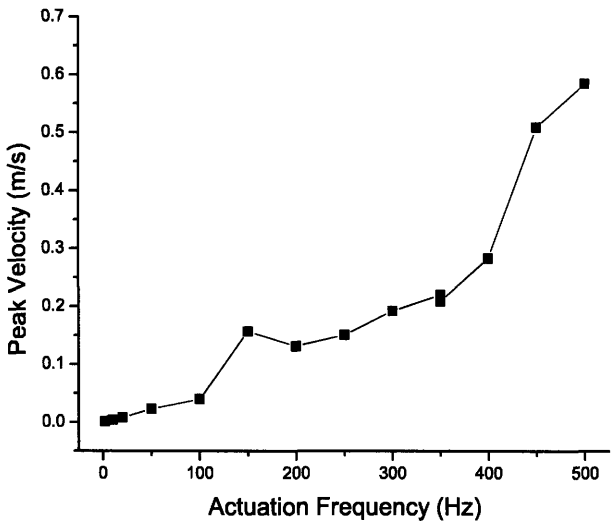

Figure 6-7: Extensional velocity of the $X4$ actuator at frequencies up to 500 Hz with the inclusion of a 12 kHz and 15 V_{rms} piezoelectric drive.

the maximum velocity occurs for an unstressed crystal that does not displace any additional mass beyond its own. This velocity is consistent with previous work by Marioni [11] that indicated the maximum velocity is approximately 6 m/s, and occurs only for an unstressed sample with a low mass ratio. The velocity falls off slowly for stresses near normal operating values (1–2 MPa) but decreases rapidly as the stress approaches the blocking stress for the crystal. The effect of increasing the mass ratio decreases the maximum velocity much more rapidly at first than does increasing the stress. The velocity is very sensitive to changes in the mass ratio for ratios near one, and becomes less sensitive as the ratio increases.

Figure 6-8 has important consequences for actuator design. The velocity puts an upper bound on the possible actuation frequency of a Ni–Mn–Ga actuator. It indicates that the FSMA should account for as much of the moving mass as possible in a high-bandwidth application. Figure 6-8 also indicates that a minimum stress should be applied for maximum bandwidth. However, in order for the FSMA crystal to fully reset following extension a minimum stress value is required. Typically, this stress is on the order of 1–2 MPa and stresses of this magnitude have only a small

impact on the peak velocity (< 10% reduction).

The analysis also indicates that the blocking stress can be found as the solution to the equation

$$0 = K_u V - S\sigma^2 V \tag{6.5}$$

from Eqn 6.4, as the peak velocity (and therefore the cyclic displacement) goes to zero at that point. Eqn. indicates that the blocking stress, σ_b, is dependent on the ratio of the maximum amount of magnetic energy that can be supplied, K_u, and the material compliance, S, as

$$\sigma_b = \sqrt{\frac{K_u}{S}} \tag{6.6}$$

The values obtained from Eqn. 6.6 agree well with the range of blocking stresses reported in the literature [21, 25].

6.3 Adaptamat Actuator Performance

Having demonstrated performance gains in output strain and lowered magnetic field threshold for twin boundary motion with acoustic assistance on laboratory devices, the technique was then applied to a small, commercially available actuator from Adaptamat. Two of the devices were acquired and one was modified as described in Chapter 3.2.4. Adaptamat #2 was modified with the inclusion of a piezoelectric within the load path to allow for acoustic assisted actuation.

In contrast to previously presented experimental data, the data presented in this section are plotted as a function of the drive current rather than magnetic field, since the design of the commercial actuator precludes direct magnetic field measurement. The magnetic field is proportional to the drive current though, by the relation

$$H = \frac{nI}{L} \tag{6.7}$$

where n is the number of magnet turns, I is the applied current, and L is the gap

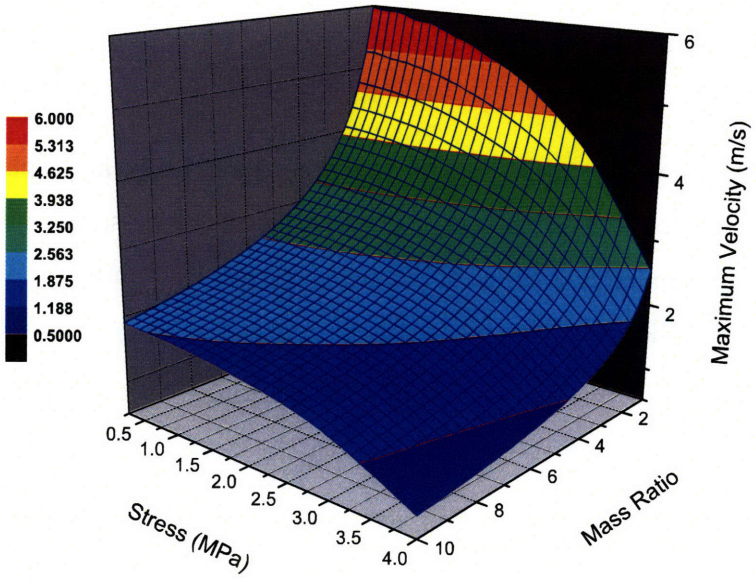

Figure 6-8: Sensitivity analysis of the peak actuator velocity as a function of applied compressive stress and the ratio of the FSMA mass to the total moving mass. Maximum velocity (bandwidth) occurs for small values of both the mass ratio and applied stress.

length for the magnet [16].

6.3.1 Adaptamat #2

Adaptamat #2 was modified to included a piezoelectric stack within the load path of the actuator. Displacement and current drive data were collected for magnetic field drive frequencies between 1 Hz and 350 Hz for the case with the piezoelectric operated at 12 kHz and 15 V_{rms} and in the absence of piezoelectric drive. The low frequency ϵ vs. I curves are plotted in Figure 6-9 and the maximum strain for all frequencies are summarized in Figure 6-10.

Figure 6-9 shows similar behavior to previous data that has been presented at low frequencies (Figure 4-8). The addition of the piezoelectric drive yields a 12% improvement in displacement output.

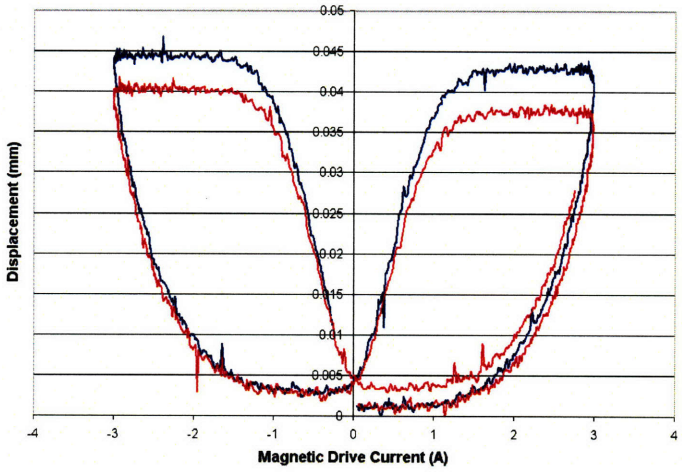

Figure 6-9: Displacement of Adaptamat #2 at 1 Hz without acoustic assist (red) and with a 12 kHz and 15 V_{rms} piezoelectric drive (blue). The addition of the piezoelectric drive adds 12% to the observed displacement.

The data in Figure 6-10 show that the displacement of the actuator is largest at the low frequencies and approximately half the displacement is lost by the 100 Hz actuation frequency. The displacement level is roughly constant from 100–400 Hz. At the higher frequencies tested, the displacement level increases noticeably over the minimum displacement. This is attributed to the resonance of the device that becomes appreciable at ≈500 Hz actuation, which corresponds to the limit of the actuator's stated operating range (Table 3.4).

With the addition of the acoustic drive, there is an improvement in the output displacement over the entire range of drive frequencies. As in the $X4$ actuator described previously, the effect is largest at low magnetic drive frequencies. At the lowest drive frequencies, the piezoelectric has 5 times the effect as it does at larger drive frequencies. This result is consistent with the previous data taken on the $X4$ apparatus which showed a similar drop-off in piezoelectric efficiency and effect with the higher magnetic drive frequencies.

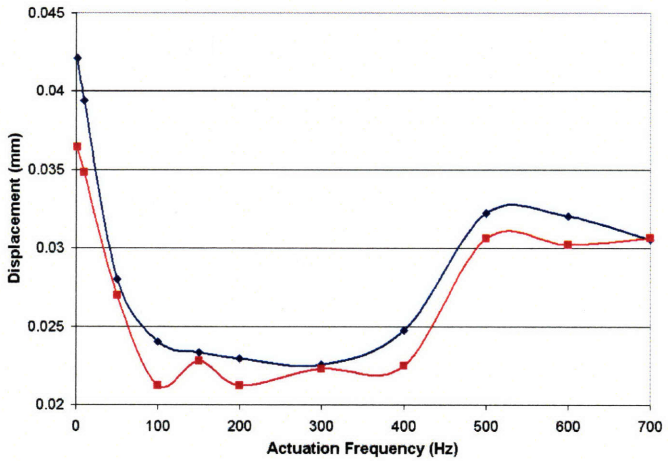

Figure 6-10: Cyclic displacement of Adaptamat #2 without acoustic assist (red squares) and with a 12 kHz and 15 V_{rms} piezoelectric drive (blue diamond). The addition of a piezoelectric drive increases the displacement output for all frequencies up to 700 Hz.

Chapter 7

Temperature Dependence

Figure 7-1 shows the strain output of the FSMA actuator at temperatures from 1–34.5 °C at 2 Hz actuation[1]. A magnetic field drive amplitude of 7200 Oe was used.

The MFIS is affected strongly by the twin-boundary mobility and the magneto-crystalline anisotropy, K_u. Each of these two quantities has a complex temperature dependence. The magneto-crystalline anisotropy, which is related to the driving force, approaches zero near the Curie temperature and increases with a decrease in temperature (Figure 1-6). Over the 35 °C temperature range of interest in this experiment however, the anisotropy is relatively constant. The twin-boundary mobility is maximum just below the austenite transformation temperature and decreases rapidly with temperature. As a result, the maximum strain is observed near the austenite start temperature ($T > 30\,°C$) for specimens studied here. The strain output decreases rapidly with a decrease in temperature. At 1 °C, the strain is almost completely suppressed.

For all temperatures, an increase in strain output is observed with the inclusion of a 12 kHz piezoelectric drive at 15 V_{rms}. Figure 7-2 shows the absolute increase in strain (strain measured as percent elongation)

$$\Delta\epsilon(T) = \epsilon_p(T) - \epsilon_0(T) \tag{7.1}$$

[1]Higher temperatures were not tested as the austenite start temperature for this sample is ≈40 °C. At this temperature the strain will approach zero as the martensite phase is replaced by austenite.

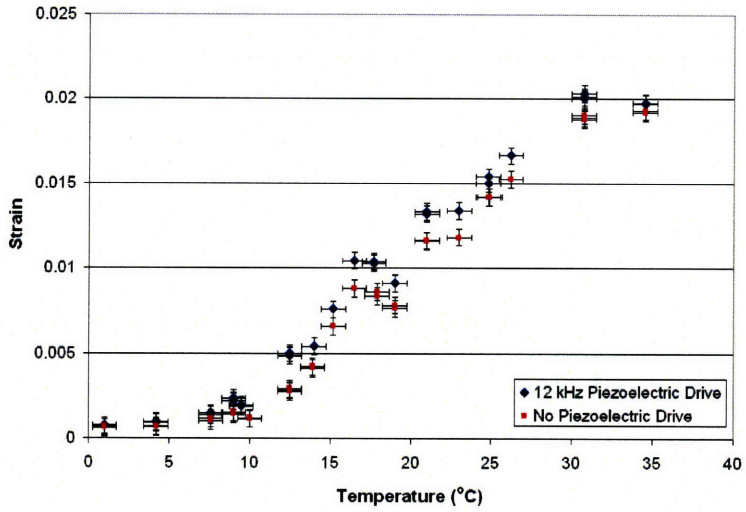

Figure 7-1: Temperature dependence of the MFIS from 1–34.5 °C without and with a 12 kHz, 15 V_{rms} piezoelectric drive.

of the crystal with the inclusion of the piezoelectric drive. In Eqn. 7.1, $\epsilon_0(T)$ is the strain without the piezoelectric drive and $\epsilon_p(T)$ is the strain with the piezoelectric drive. Figure 7-3 shows the percent change in strain output where

$$\%\Delta\epsilon = 100 \times \frac{\epsilon_p(T) - \epsilon_0(T)}{\epsilon_0(T)} \tag{7.2}$$

with the addition of the piezoelectric drive, relative to the strain without the piezoelectric drive. For absolute gain in strain, the largest improvements of ≈0.02% strain are found for 12 °C and tend to decrease slowly with decreasing or increasing temperature. This also coincides with the largest percentage gain in strain relative to the strain without the piezoelectric. Due to the rapid increase in strain with temperature, the relative change in strain, ϵ_0, is maximum around 12 °C and decreases rapidly as the temperature is raised further.

The gain from the piezoelectric, in both absolute and relative terms, is suppressed at low temperatures/mobility and for high temperature/mobility. Near the austenite start temperature, the material stiffness is minimized (Figure 1-8) and the thermal agitation is high. The twins are free to move in the absence of the piezoelectric

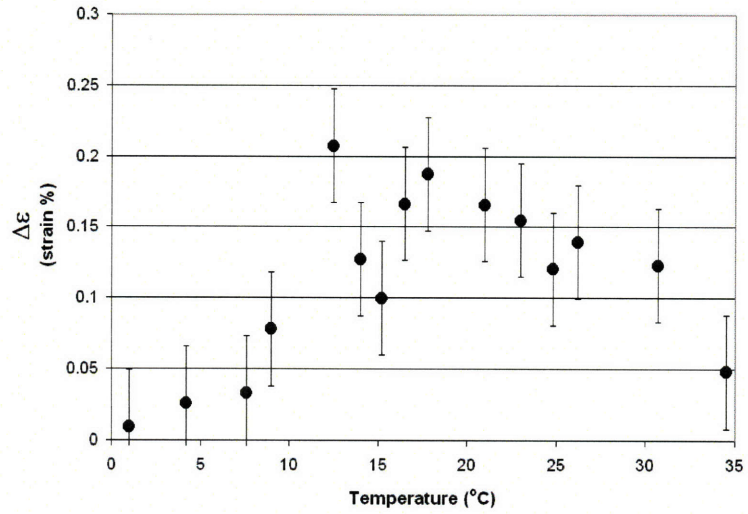

Figure 7-2: Absolute change in strain output (strain %) with the addition of a piezoelectric drive for operating temperatures of 1–34.5 °C.

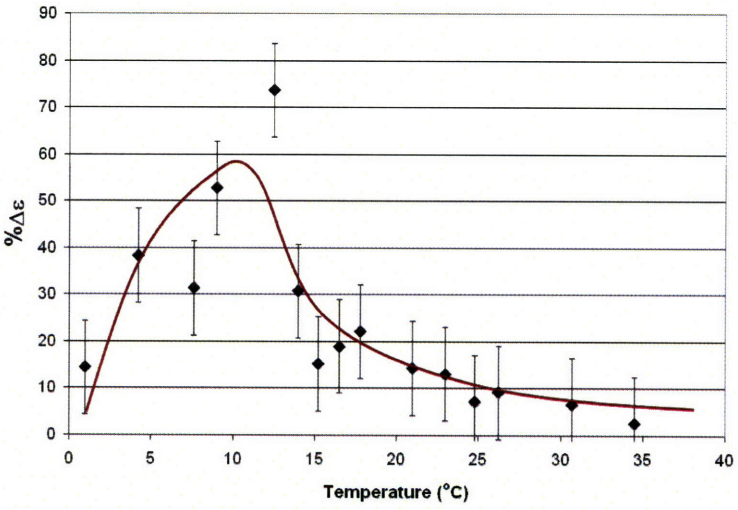

Figure 7-3: Percent change in strain output (relative) with the addition of a piezoelectric drive for operating temperatures of 1–34.5 °C.

drive, so the relative gains are small with the addition of the piezoelectric drive in this region. For the lowest temperatures, the twin-mobility is very low in the absence of the piezoelectric drive and the piezoelectric is limited by this low inherent mobility. The temperatures tested were sufficiently below the Curie temperature such that the magneto-crystalline anisotropy is weakly dependent on temperature and the temperature change has a weak effect on the driving force.

Chapter 8

Summary, Conclusions, and Future Work

8.1 Summary

A series of experiments has been performed to evaluate the effect of a piezoelectric drive on the magnetic-field-induced strain in Ni–Mn–Ga for the first time. Three separate experimental apparatuses were constructed and used to collect data. The first of these was a low-frequency apparatus based on the $X1$ magnet used by C. Henry [25]. The $X1$ apparatus was used to collect data on the effect of the piezoelectric at 1 Hz magnetic-field-induced actuation at various piezoelectric operating conditions. The $X4$ apparatus incorporated a magnet that is capable of producing magnetic fields at frequencies high enough for actuation at 500 Hz. The apparatus was modeled using ANSYS® Workbench to determine the resonant modes of the system and optimize the design for higher-frequency operation. The $X4$ design was also placed in an insulated container to allow for temperature dependent measurements to be conducted. The third apparatus used was based on a commercial product by Adaptamat, Inc. The compact, commercial actuator was modified by including a piezoelectric stack within the load path to allow for the evaluation of the piezoelectric drive on a device meant for real-world application.

Experiments conducted at 1 Hz actuation on the $X1$ apparatus have shown that the change in output strain is dependent on the maximum magnetic drive field that is used relative to the threshold field for twin-boundary motion. For maximum magnetic field values just below threshold, the application of a piezoelectric drive causes an 800% increase in strain relative to the case without the piezoelectric drive. The same piezoelectric drive with a magnetic field $\approx$250 Oe above the threshold, causes a 68% increase in strain.

With a magnetic field drive capable of saturation ($\geq$8000 Oe), the change in strain with the piezoelectric drive is diminished. Experiments with a piezoelectric drive at 5 kHz and 20.3 V_{rms} on a sample from TL7, showed an increase in absolute strain of 0.0024. The crystal sample from TL7 also showed a large reduction in threshold of 1000 Oe with the 5 kHz piezoelectric drive. Stress output was shown to be essentially unchanged with the addition of a piezoelectric drive. When the same experiment was performed on a low-defect sample from TL8, the threshold reduction was shown to be on the order of 200 Oe for a similar piezoelectric drive.

A finite element model of the $X4$ apparatus was constructed and used by ANSYS® Workbench to determine the resonant modes of the system. The models were used to optimize system design to allow for operation under a wide range of actuation frequencies. On the design used for data collection, the first resonant mode identified by ANSYS® was at 580 Hz, allowing for data collection at actuation frequencies up to 500 Hz.

Data collected at frequencies up to 500 Hz on the $X4$ apparatus showed overall strain improvement with the addition of the piezoelectric drive. The effect of the added piezoelectric drive was most pronounced at frequencies below 50 Hz.

The temperature dependence of the effect of the piezoelectric drive was also investigated from 0–34.5 °C. For all temperatures, the piezoelectric drive caused an increase in strain. The maximum effect was observed for temperatures near 15 °C, and diminished effects near 0 °C and 34.5 °C.

8.2 Conclusions

The piezoelectric drive has been shown to improve the output strain and lower the magnetic threshold to initiate twin-boundary motion in Ni–Mn–Ga. The effectiveness of the piezoelectric in increasing strain output and lower threshold field depends on the temperature, maximum magnetic field amplitude used to drive the FSMA, and the initial defect concentration within the FSMA.

Low-frequency data indicated that the gain in strain output with the inclusion of the piezoelectric drive is largest for magnetic field drives near the threshold field. The piezoelectric causes a reduction in the threshold field and therefore large changes are seen when the maximum magnetic field is near the threshold. This large change in threshold is what accounts for the large increases in strain output (up to a 800% increase) for magnetic field drives near the threshold. With a large magnetic field drive, near the saturation value, the change in strain with the addition of the piezoelectric drive is less dramatic. For large drive fields, the strain output in the absence the piezoelectric drive is near the maximum theoretical value, therefore the potential gains with the addition of a piezoelectric drive are smaller.

The change in threshold reduction between TL7 and TL8 with the addition of the piezoelectric drive, indicates that the defect structure in the material is important in determining the effectiveness of the piezoelectric drive. The sample from TL7 contains significant amounts of retained austenite and has an initially large threshold while TL8 has a low concentration of defects [43, 46]. For samples with large defect concentrations, the piezoelectric drive is capable of assisting the magnetic field in overcoming the defects to a large extent and enables the twin-boundaries to move throughout the crystal. This results in the largest changes in threshold and output strain. Low defect samples with initially low threshold fields, show small gains in output stain and small reductions in threshold field as there are fewer defects for the piezoelectric drive to act upon.

The temperature is also important in determining the extent of the effect that the piezoelectric drive has on the actuation of Ni–Mn–Ga. The magneto-crystalline

anisotropy and mechanical stiffness are important in determining the extent of the magnetic-field-induced strain and both vary with temperature. The maximum effect of piezoelectric assist on field induced actuation is seen at around 15 °C. This is a result of the inherently large twin mobility at temperatures near the austenite start temperature which limits the gains from the piezoelectric drive. At lower temperatures, the anisotropy is largest which results in the large driving forces. However, the material stiffness is larger and twin mobility and thermal energy are inherently low at suppressed temperatures. The low thermal energy and mobility are too great an effect for the piezoelectric drive to overcome.

Analysis of the power requirements and efficiency were performed. By considering the magnetic work input and mechanical input from the piezoelectric drive to the FSMA and the mechanical output of the FSMA, an estimate of the efficiency of the device was found. The magnetic power input is substantially greater than the mechanical power input supplied from the piezoelectric. The analysis indicated that the addition of the piezoelectric drive can increase the efficiency by $\approx$0.5% on a sample from TL7 that is operated with magnetic fields of $\pm$8000 Oe. The gain in efficiency is mainly the result of increased strain output. Therefore, larger gains in efficiency are possible with smaller magnetic field magnitudes, especially with maximum magnetic field drive amplitude near threshold as the increase in strain is maximized in this region.

Measurements of the effect of the piezoelectric drive at varying FSMA actuation frequencies indicated the largest effect occurs at FSMA actuation frequencies below 50 Hz. At higher frequencies, the effect is diminished as a result of the dynamic response of the system becoming the limiting factor. Also, the decrease in the ratio of piezoelectric drive cycles to FSMA actuation cycles may also play a role.

Modeling and experimental results also give interesting conclusions relating to actuator design. The power requirements to operate a magnetic actuator scale with the square of the required magnetic field (Eqn. 1.10). The piezoelectric drive can therefore allow for a large reduction in magnetic power required to achieve a desired actuation level. Analysis of the high-frequency data has indicated that the bias stress

and the ratio of the total mass of the moving parts to that of the FSMA are both important in determining the maximum actuation velocity of the FSMA. The highest actuation velocities (and therefore actuation frequencies) are obtained for devices with low mass ratios and relatively low bias stresses.

8.3 Future Work

The measurements presented in this thesis were the first taken showing the effect of a piezoelectric drive on the magnetic-field-induced strain from Ni–Mn–Ga ferromagnetic shape memory alloys. As a result, there are a number of avenues of future work that arose.

- During this research, the dependence of the ratio of the piezoelectric drive frequency to the FSMA actuation frequency arose as a potentially useful quantity. In performing the actuation frequency measurements on the $X4$ apparatus, it was observed that the effect of the piezoelectric (when operated at a constant piezoelectric drive frequency) decreased with increasing magnetic actuation frequency. The reduction may have been a result of fewer excitations from the piezoelectric per FSMA actuation cycle at high actuation frequencies. Testing the effect of the piezoelectric drive at a fixed ratio of the piezoelectric frequency to the actuation frequency is therefore of interest.

- This research has indicated a correlation between defect strength, threshold, and the extent of the effect the piezoelectric drive has on the actuation properties. To date, however, the correlation has been determined for samples from two crystal boules giving a limited range of defect types. It would be useful to study other samples and work toward a better understanding of the mechanisms by which different defects interact with twin disloactions.

- Marioni [11] was able to determine the magnetic field required to initiate twin-boundary motion on multiple twin-boundaries via optical measurement. Repeating those experiments with the addition of a piezoelectric drive may give

interesting insight into what range of defect strengths the piezoelectric drive is most effective in aiding the magnetic field.

- Ferromagnetic shape memory alloys have large power outputs at frequencies below roughly 1 kHz, while piezoelectric stacks have large power outputs at frequencies in the 10s of kHz. The combination of a ferromagnetic shape memory alloy and a piezoelectric stack gives the possibility of developing a hybrid, broadband transducer. There is still much to be learned about the potential technical benefits of combining piezoelectric and FSMA actuators in hybrid devices.

Bibliography

[1] R. D. James and D. Kinderlehrer. Theory of magnetostriction with applications to $Tb_xDy_{1-x}Fe_2$. *Phil. Mag. B*, 68:237 – 274, 1993.

[2] R. D. James and M. Wuttig. Alternative smart materials. *SPIE*, 2715:420–426, 1996.

[3] K. Ullakko, J. K. Huang, C. Kantner, R. C. O'Handley, and V. V. Kokorin. Large magnetic-field-induced strains in Ni_2MnGa single crystals. *Appl. Phys. Lett.*, 69:1966 – 1968, 1996.

[4] K. Ullakko, J. K. Huang, V. V. Kokorin, and R. C. O'Handley. Magnetically controlled shape memory effect in Ni_2MnGa intermetallics. *Scripta Mater.*, 36:1133–1138, 1997.

[5] G. H. Wu, C. H. Yu, L. Q. Meng, F. M. Yang, S. R. Qi, W. S. Zhan, Z. Wang, Y. F. Zheng, and L. C. Zhao. Giant magnetic-field-induced strains in Heusler alloy NiMnGa with modified composition. *Appl. Phys. Lett.*, 75:2990–2992, 1999.

[6] R. D. James, R. Tickle, and M. Wuttig. Large field-induced strains in ferromagnetic shape memory materials. *Mat. Sci. Eng. A*, 273-275:320–325, 1999.

[7] R. Tickle and R. D. James. Magnetic and magnetomechanical properties of Ni_2MnGa. *J. Magn. Mag. Mat*, 195:627–638, 1999.

[8] S. J. Murray, M. A. Marioni, S. M. Allen, R. C. O'Handley, and T. A. Lograsso. *Appl. Phys. Let.*, 77:886, 2000.

[9] A. Sozinov, A. A. Likhachev, N. Lanska, and K. Ullakko. Giant magnetic-field-induced strain in nimnga seven-layered martensitic phase. *Appl. Phys. Lett.*, 80:1746 – 1748, 2002.

[10] R. W. Overholser, M. Wuttig, and D. A. Neumann. Chemical ordering in Ni–Mn–Ga Heusler alloys. *Scripta Mater.*, 40:1095–1102, 1999.

[11] Miguel A Marioni. *Pulsed magnetic field-induced twin boundary motion on Ni-Mn-Ga.* PhD thesis, Massachusetts Institute of Technology, Cambridge, MA, May 2003.

[12] G. B. Olson and W. S. Owen. *Martensite.* ASM International, 1992.

[13] R.J.Biermann D.E.Hodgson, M.H.Wu. *Metals Handbook*, volume 2. ASM International, 1990.

[14] R. E. Reed-Hill and R. Abbaschian. *Physical Metallurgy Principles.* PWS Publishing Company, Boston, 3 edition, 1994.

[15] J.M. Chambers. Design and characterization of acoustic pulse shape memory alloy actuators. Master's thesis, M.I.T., 2005.

[16] R. C. O'Handley. *Modern Magnetic Materials.* John Wiley & Sons, Inc., New York, 2000.

[17] L. Straka and O. Heczko. Magnetic anisotropy in Ni–Mn–Ga martensites. *J. App. Phys.*, 93(10), May 2003.

[18] L. Dai, J. Cullen, and M. Wuttig. Intermartensitic transformation in a nimnga alloy. *J. Appl. Phys.*, 95(11), June 2004.

[19] L. Dai, J. Cullen, J. Cui, and M. Wuttig. Elasticity study in ferromagnetic shape memory alloys. volume 785. Materials Research Society, Materials Research Society, Fall 2004.

[20] O. Heczko and L. Straka. Temperature dependence and temperature limits of magnetic shape. *J. Appl. Phys.*, 94(11):7139, Dec 2003.

[21] S. J. Murray, M. Marioni, P. G. Tello, S. M. Allen, and R. C. O'Handley. Giant magnetic-field-induced strain in Ni–Mn–Ga crystals: experimental results and modeling. *J. Magn. Mag. Mat*, 226:945–947, 2001.

[22] R. C. O'Handley. Model for strain and magnetization in magnetic shape-memory alloys. *J. Appl. Phys.*, 83:3263–3270, 1998.

[23] C. P. Henry, J. Feuchtwanger, D. Bono, R. C. O'Handley, and S. M. Allen. AC magnetic field-induced strain of single crystal Ni–Mn–Ga. In *Smart Structures and Materials 2002*, San Diego, USA, 2002.

[24] C. P. Henry, J. Feuchtwanger, D. Bono, M. A. Marioni, P. G. Tello, M. Richard, S. M. Allen, and R. C. O'Handley. AC performance and modeling of ferromagnetic shape memory actuators. In *Smart Structures and Materials 2001*, volume SPIE 4333, pages 151–161, Newport Beach, USA, 2001.

[25] C. P. Henry. *Dynamic Actuation Properties of Ni–Mn–Ga Ferromagnetic Shape Memory Alloys.* PhD thesis, M.I.T., Cambridge, MA, May 2002.

[26] C. P. Henry, J. Feuchtwanger, D. Bono, M. A. Marioni, P. G. Tello, M. Richard, S. M. Allen, and R. C. O'Handley. Ac performance and modelling of ferromagnetic shape memory actuators. In *Smart Structures and Materials*, volume Proceedings of SPIE Vol. 4333, pages 151–162, 2001.

[27] S. J. Murray. *Magneto-mechanical properties and applications of Ni–Mn–Ga ferromagnetic shape memory alloy.* PhD thesis, M.I.T., Cambridge, MA, January 2000.

[28] M.J.Hoffmann and K.Kungl. High strain lead-based perovskite ferroelectrics. *Current Opinion in Solid State and Materials Science*, 8(1):51–57, Jan. 2004.

[29] G.H. Haertling. Ferroelectric ceramincs: History and technology. *J. Am. Ceram. Soc.*, 82(4):797–818, 1999.

[30] J.F.Nye. *Physical Properties of Crystals.* Oxford Science Publicaitons, 2nd edition, 2000.

[31] O.Saburi. Properties of semiconductive barium titanates. *J. Phys. Soc. Jpn*, 14(9):159–1174, 1984.

[32] G.H.Haertling and C.E.Land. Recent improvements in the optical and electrooptic properties of PLZT ceramics. *Ferroelectrics*, 3:269–280, 1972.

[33] W. J. Dawson. Hydrothermal synthesis of advanced ceramic powders. *Am. Ceram. Soc. Bull.*, 67(10):1673–38, 1988.

[34] Piezo Systems. *Piezoelectric Stack Actuator Technical Specifications*, 2006.

[35] B. W. Peterson, J. Feuchtwanger, J. M. Chambers, D.Bono, S. R. Hall, S.M. Allen, and R. C. O'Handley. Acoustic assisted, field-induced strain in ferromagnetic shape memory alloys. *J. Appl. Phys.*, 95:6963–6964, 2004.

[36] R. C. O'Handley, D. I. Paul, M. A. Marioni, C. P. Henry, M. Richard, P. G. Tello, and S. M. Allen. Field-induced strain in ferromagnetic shape memory actuators: from macroscopic to microscopic models. In *The Fourth Pacific Rim International Conference on Advanced Materials and Processing*, volume PRICM4, pages 2945–2948, 2001.

[37] S. M. Allen M. Richard J. Feuchtwanger B. Peterson R. Techapiesancharoenkij M. Barandiarán P. Lázpita R. C. O'Handley, D. I. Paul. Model for temperature dependence of field-induced strain in ferromagnetic shape memory alloys. *submitted for pub.*

[38] D. I. Paul. Theory of magnetization: Twin boundary interaction in ferromagnetic shape memory alloys. *J. Appl. Phys.*, 93(8):4561, April 2003.

[39] D.I. Paul, R.C. O'Handley, and B.W. Peterson. Ferromagnetic shape memory alloys: Theory of interactions. *J. Appl. Phys.*, 97(10), May 2005.

[40] E. Callen H.B. Callen. *J. Phys. Chem. Sol.*, 27:1271 – 1285, 1966.

[41] W.Q.Wang et al. Z.H. Liu, M. Zhang. Magnetic properties and martensitic transformation in quaternary heusler alloy of NiMnFeGa. *J. Appl. Phys.*, 92(9):5006–5010, 2002.

[42] M. A. Marioni. Nonuniform twin-boundary motion in Ni-Mn-Ga single crystals. *APL*, 84(20), May 2004.

[43] M.L. Richard. *Systematic analysis of the crystal structure, chemical ordering, and microstructure of Ni-Mn-Ga ferromagnetic shape memory alloys.* Ph.D thesis, M.I.T., Cambridge, MA, August 2005.

[44] D. L. Schlagel, Y. L. Wu, W. Zhang, and T. A. Lograsso. *J. Alloys Comp.*, 312:77, 2000.

[45] X. Jin, M. A. Marioni, D. Bono, S. M. Allen, R. C. O'Handley, and T. Y. Hsu. Empirical mapping of Ni–Mn–Ga properties with composition and valence electron concentration. *J. Appl. Phys.*, 91(10):8222 – 8224, 2002.

[46] M. Richard. unpublished results, 2006.

[47] X. Du Q. Wang. Electromechanical coupling and output efficiency of piezoelectric bending acutators. *IEEE Transactions on ultrasonics, ferroelectrics, and frequency control.*, 46(3):638–646, May 1999.

[48] C. Rogers V. Giurgiutiu and Z. Chaudhry. Energy-based comparison of solid-state induced-strain actuators. *J. Of Intelligent Material Systems and Structures*, 17(1):4–14, Jan. 1996.